

國立臺灣大學電機資訊學院電信工程學研究所



博士論文

Graduate Institute of Communication Engineering

College of Electrical Engineering and Computer Science

National Taiwan University

Doctoral Dissertation

經驗模態分解中突波問題的解決架構

A solution framework for spike problem in empirical mode
decomposition

楊惠雯

Hui-Wen Yang

指導教授：鄭士康博士、羅孟宗博士

Advisor: Shyh-Kang Jeng, Ph.D. and Men-Tzung Lo, Ph.D.

中華民國 109 年 5 月

May, 2020



國立臺灣大學 (碩) 博士學位論文
口試委員會審定書

經驗模態分解中突波問題的解決架構
A Solution Framework for Spike Problem in Empirical
Mode Decomposition

本論文係楊惠雯君 (D03942010) 在國立臺灣大學電信工程學研究所完成之碩 (博) 士學位論文，於民國 109 年 5 月 26 日承下列考試委員審查通過及口試及格，特此證明

口試委員：

鄭士康 (簽名)
(指導教授)

林亮宇 黃冠

羅志宇 王淵弘

所 長

蔡水原 (簽名)

謝辭

原來真的很不容易。

謝謝鄭老師啟發性的指引，教我做學問的方法，他給學生的不是魚也不是桿，是找池塘的方法。謝謝羅老師七年來的栽培，他總是有很多神奇的點子。謝謝王淵弘老師、楊緒文老師對 EMD 的數學性質的建立，我才能站在巨人的肩膀上。謝謝林激老師亦師亦兄的指導，他在醫學、數學、電機方面的跨領域長才，是我向前奔跑的目標。謝謝合作的醫生們，包括台大的林亮宇教授、北醫心臟內科的施俊明、黃群耀和蕭成儀醫師、北榮的林彥璋醫師和國泰醫院的王晨旭醫師。也謝謝口委黃文良老師，拜讀他的文章總是能有新的領悟。

謝謝一直在身邊支持我的家人、學長學弟、朋友、酒友、跑友、和在天上的嘟嘟。和人聊到自己在攻讀博士時，常聽到的回應是說妳一定很聰明或是很喜歡唸書。其實沒有。我只是很幸運又很任性，為了強化自己沒有的技能，把自己的人生登入了一個叫博士學位的 RPG 遊戲裡，強迫自己每天練功打怪，每半年還要被國立台灣大學課金一次。雖然花了比預期還長的時間，今天終於登出遊戲了。最後謝謝自己那些熬的夜和換不回的青春，謝謝這一切。



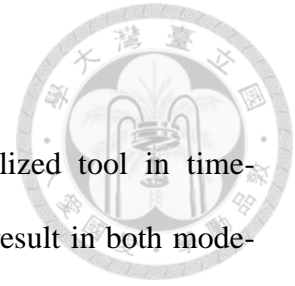
中文摘要



經驗模態分解是一個被廣為使用的時頻分析工具，然而，訊號中的雜訊干擾，例如突波，可能同時造成模態混合和模態分裂的問題，使得一個物理上有意義的成份被拆解成二個以上的本質模態函數。在此論文中，我們引用近期發展出的經驗模態分解的數學理論，提供突波問題造成模態混合和模態分裂的理論解釋，並且基於此理論基礎，提出了解決突波問題的架構——最小弧長條件。為了更穩健地將突波分離至原先不存在的本質模態函數中，我們加入了以弦波輔助的遮罩方法，而形成了「遮罩—最小弧長—經驗模態分解」。在論文中提供了此方法的數學理論和數值模擬，並且應用至真實世界的訊號，包括電流中的突波干擾、軸承震動訊號、睡眠腦波中的週期性交替模式和核心體溫的生理時鐘。更有甚者，我們將此方法應用在標準十二導心電圖上以分離 P 波的波形，並且證明由此 P 波波形所提取的特徵，可以用來偵測受測者是否有潛在的心房顫動。最後，我們將此方法延伸至單位階梯函數上，並且提出一個廣適性的演算法，來處理第 N 階導數為突波的訊號。

Abstract

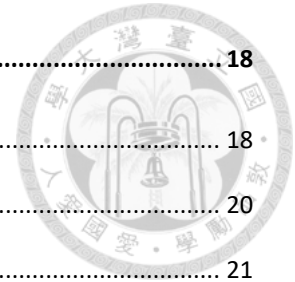
Empirical mode decomposition (EMD) is an extensively utilized tool in time-frequency analysis. However, disturbances such as impulse noise can result in both mode-mixing and mode-splitting effect, in which one physically meaningful component is split in two or more intrinsic mode functions (IMFs). In this work, we provide a mathematical explanation for the cause of mode-mixing and mode-splitting by spikes in EMD, and propose a novel method, the minimum arclength EMD (MA-EMD), to robustly decompose time series data with spikes. To further isolate the spike in a previously non-existent IMF, the masking-aided MA-EMD (MAMA-EMD) is provided. The mathematical foundations and limitations for these two methods are provided. The MAMA-EMD is utilized to deal with four real-world data including electrical current, vibration signals, cyclic alternating pattern in sleep EEG (Electroencephalography), and circadian of core body temperature. In addition, this work developed a tool for P-wave isolation in electrocardiogram (ECG) by the MAMA-EMD method, and showed that the P-wave related features can be used to identify potential atrial fibrillation patients. Finally, we extend our application to the Heaviside step function and propose a general algorithm for signals whose Nth order derivative is a spike function.



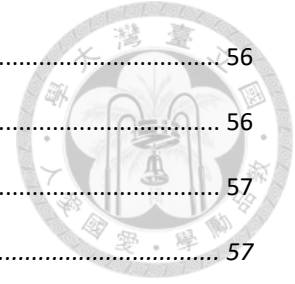
Contents



謝辭.....	I
中文摘要.....	II
ABSTRACT	III
CONTENTS	IV
LIST OF FIGURES.....	VII
LIST OF TABLES.....	X
CHAPTER 1. INTRODUCTION	1
1.1 STATEMENT OF PURPOSE	1
1.2 CONTRIBUTION	2
1.3 RELATED WORKS	3
1.3.1 EMD and time-frequency decomposition	3
1.3.2 Modifications of EMD	5
1.4 SPIKE PROBLEMS.....	7
1.4.1 Spike problems in signal processing.....	7
1.4.2 Spike problems in EMD.....	7
1.5 OVERVIEW.....	9
CHAPTER 2. BACKGROUND	11
2.1 EMD.....	11
2.2 IMPULSE RESPONSE OF EMD.....	11
2.3 MODE-MIXING AND MODE-SPLITTING	14
2.4 MASKING EMD	15
2.5 THE SPIKE DETECTION.....	16



CHAPTER 3. EFFECT ANALYSIS OF SPIKE IN EMD AND MA-EMD	18
3.1 EFFECT ANALYSIS OF SPIKE PROBLEM IN EMD	18
3.2 MSI: MEASUREMENT OF MODE-SPLITTING	20
3.3 NE: NEWLY GENERATED EXTREMA.....	21
3.4 SK-EMD: SKIPPING THE EXTREMA ON SPIKES.....	21
3.5 MA-EMD	22
3.5.1 <i>Minimum arclength criterion</i>	22
3.5.2 <i>Mathematical foundation</i>	24
3.5.3 <i>Simulation verification</i>	25
3.5.4 <i>Comparative accuracy analysis</i>	31
3.6 COMPARISON BETWEEN SKIP AND MA-EMD	34
CHAPTER 4. MASKING-AIDED MINIMUM ARCLENGTH EMD.....	36
4.1 INTRODUCTION.....	36
4.2 DETERMINATION OF MASKING SIGNAL.....	37
4.3 SIMULATION VERIFICATION	39
4.3.1 <i>Single Sinusoid</i>	39
4.3.2 <i>DUFFING WAVE</i>	42
4.4 LIMITATIONS	44
4.5 EXAMPLES	45
4.5.1 <i>Electrical current</i>	45
4.5.2 <i>Rotor test rig</i>	48
4.5.3 <i>Cyclic alternation pattern subtype classification in sleep electroencephalography</i>	51
CHAPTER 5. APPLICATION OF MAMA-EMD ON P-WAVE EXTRACTION FOR DETECTION OF POTENTIAL	
ATRIAL FIBRILLATION PATIENTS.....	56



5.1 SIGNIFICANCE FOR AF DETECTION	56
5.2 RECENT WORKS RELATED TO AF DETECTION UNDER SINUS RHYTHM.....	56
5.3 METHOD FOR P-WAVE ANALYSES	57
5.3.1 Subject selection.....	57
5.3.2 ECG Signal processing	59
5.3.3 Feature extraction.....	63
5.3.4 Statistical analysis.....	66
5.4 STATISTICAL SIGNIFICANCE OF THE FEATURES	67
5.4.1 Morphology features	67
5.4.2 PCA related features	69
5.4.3 Inter-lead P-wave dispersion.....	69
5.5. CLASSIFICATION OF AF AND CONTROL PATIENTS.....	70
5.6 DISCUSSION AND IMPLICATION.....	72
CHAPTER 6. EXTENSION TO STEP FUNCTION	75
6.1 GENERALIZED ALGORITHM	75
6.2 EXAMPLE: PHOTOPLETHYSMOGRAM (PPG) RECORDING	76
CHAPTER 7. CONCLUSION	80
BIBLIOGRAPHY.....	82



List of Figures

Figure 1- 1. Surrogated nonstationary Duffing signal contaminated by triangular spikes, and its decomposition by EMD and our proposed MAMA-EMD, respectively.....	2
Figure 1- 2. Decomposing a sinusoid wave with a spike using different modifications of EMD (a) EEMD. (b) CEEMDAN. (c) UPEMD. (d) MA-EMD.	9
Figure 2- 1. The upper envelope, spline curves, and the effect of a spike.	13
Figure 3- 1. The spike-interrupted Duffing wave and its decomposition by different methods.....	20
Figure 3- 2. Optimal replacement (pentagram) of spike point (A) found using the minimum arclength criterion.....	24
Figure 3- 3. Simulation 1: decomposing a two-tone signal with spikes of different heights and positions.	26
Figure 3- 4. The results of simulation 1 by EMD.....	27
Figure 3- 5. The results of simulation 1 by MA-EMD.....	28
Figure 3- 6. Simulation 2: decomposing a randomly generated low-frequency signal with a high-frequency sinusoid and a spike of different heights.....	29
Figure 3- 7. The results of simulation 2 by EMD (black) and MA-EMD (red).....	30
Figure 3- 8. Comparative accuracy analysis: decomposing a sinusoid with a spike under different SNRs using EMD, MA-EMD, and UPEMD. The SNR = 0 dB in this example...	32
Figure 3- 9. The results of the comparative accuracy analysis.....	33



Figure 3- 10. The CBT data and the results from different methods..... 35

Figure 4- 1. The simulated signal and its decomposed IMFs..... 40

Figure 4- 2. The MSE of IMF2 extracted by MAMA-EMD for different fM and aM . The ground truth is a pure sinusoidal signal..... 41

Figure 4- 3. Surrogated nonstationary Duffing signal contaminated by triangular spikes, and its decomposition by EMD and our proposed MAMA-EMD, respectively..... 43

Figure 4- 4. Hilbert spectrum showing the frequency overlapping caused by spikes..... 44

Figure 4- 5. Electrical current data..... 47

Figure 4- 6. Intrinsic mode functions of the electrical current data (IMFs) derived from EMD (a) and MAMA-EMD (b)..... 48

Figure 4- 7. A vibration signal from bearing 3 with inner race defect..... 50

Figure 4- 8. Intrinsic mode functions (IMFs) derived from EMD (a) and MAMA-EMD (b).
..... 50

Figure 4- 9. Envelope spectra of components derived from EMD (a-b) and MAMA-EMD (c-d)..... 51

Figure 4- 10. An example of CAP cycles in 4 EEG channels (Fp2-F4, F4-C4, C4-P4 and P4-O2)..... 53

Figure 4- 11. An example of CAP cycles. A CAP cycle is defined as a sequence of 2 alternating EEG patterns called phase A (indicated by red line) and phase B..... 54

Figure 4- 12. Proportion of time that the extracted spikes in a phase A exceed the threshold.
..... 55

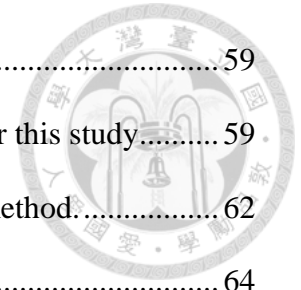


Figure 5- 1. Subject selection diagram. 59

Figure 5- 2. Flowchart for the ECG processing and feature extraction for this study..... 59

Figure 5- 3. The isolation of P-wave by applying twice the MA-EMD method..... 62

Figure 5- 4. The PCA transform for 8 of the 12 leads..... 64

Figure 5- 5. The P-loop descriptor by PC1 and PC2..... 65

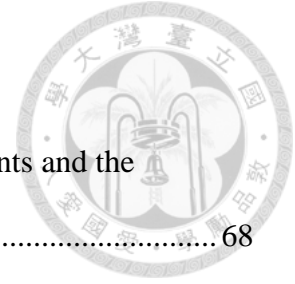
Figure 5- 6. The inter-lead correlation of the P-loop by PC1, PC2 and PC3. 66

Figure 5- 7. The ROCs for classifying AF patients by single variable. 71

Figure 5- 8. The ROC for classifying AF with combined variables..... 72

Figure 6- 1. Step function removal in PPG using MA-EMD. 78

Figure 6- 2. Flowchart for removing step functions in the PPG signal. 79



List of Tables

Table 5- 1. Differences in morphology features for AF and control patients and the respective hazard ratio in cox survival analysis.	68
Table 5- 2. Differences in PCA related features for AF and control patients and the respective hazard ratio in cox survival analysis.	69
Table 5- 3. Differences in inter-lead P-wave dispersion for AF and control patients and the respective hazard ratio in cox survival analysis.	70
Table 5- 4. The top 10 features for classifying the AF and control subjects when single feature is used.	71
Table 5- 5. The first 5 selected feature for classifying AF patients using stepwise forward selection in the logistic regression.	72

Chapter 1. Introduction



1.1 Statement of purpose

Empirical mode decomposition (EMD) is a powerful and popular tool to decompose a time series into several intrinsic mode functions (IMFs), and has been widely utilized for non-linear and non-stationary signals. Spikes are extremely high/low values in very short periods in time-domain but contain wide spectrums of frequency. When decomposed by EMD, the energy of a single spike would propagate to nearby signal and be scattered in several IMFs with different frequencies. Even though locality characteristic of EMD permits its effect to decay exponentially [1], the relatively strong magnitude of spike still results in perturbation of the IMF. Fig. 1-1(a-b) shows an example of Duffing wave with spikes decomposed by EMD. Compared to the IMFs from the same Duffing wave without spikes, the ~ 0.1 Hz signal is split into IMF 1 and 2. This is called the mode-splitting effect.

In this work, we provide a novel method, MA-EMD to solve the spike problem in EMD. Combining with masking signal to become masking-aided MA-EMD (MAMA-EMD), we successfully isolate the spikes in the first IMF, and leave the later decomposition free from interferences (Fig. 1-1(c)). In another aspect, we can regard spikes as information to be extracted, such as the delta waves in EEG and the P-wave in ECG, and further analyze the extracted waves.

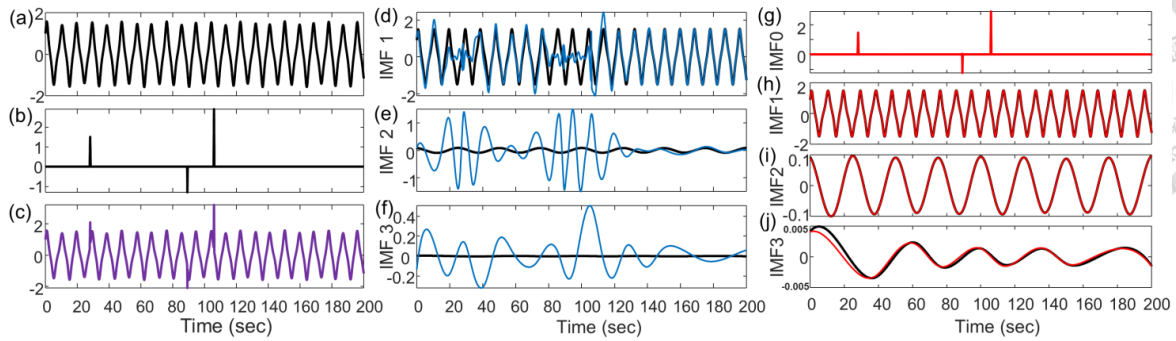


Figure 1- 1. Surrogated nonstationary Duffing signal contaminated by triangular spikes, and its decomposition by EMD and our proposed MAMA-EMD, respectively.

(a) Duffing wave. (b) The spike signal as a perturbation. (c) The spike-contaminated signal as the input for EMD and MAMA-EMD. (d-f) The blue lines are results of EMD on (c), and the black lines are from EMD on pure Duffing wave in (a) as the ground truth. (g-h) The red lines are MAMA-EMD on (c). The black lines in (h-j) are the same as the black lines in (d-f) but in different scales. Note that with MAMA-EMD method, the triangles are extracted, and the mode-splitting effect in (d-e), in which the 0.1Hz component in the first IMF of black line is split into IMF 1 and 2, is alleviated.

1.2 Contribution

- A novel method, named minimum-arclength EMD (MA-EMD) is proposed to solve the effect of spikes in EMD.
- The effect of spike and the cause of mode-mixing and mode-splitting in EMD is analyzed mathematically by recently developed impulse response theory.
- The theoretical foundation for the proposed MA-EMD is provided and supported by numerical simulations.
- The masking-aided MA-EMD (MAMA-EMD), which combines masking EMD and MA-EMD, is proposed to improve the extraction of spikes.
- Using MAMA-EMD, we showed that the extracted P-wave in 12-lead ECG can provide important features for identifying potential atrial fibrillation patients during sinus rhythm.



1.3 Related works

1.3.1 EMD and time-frequency decomposition

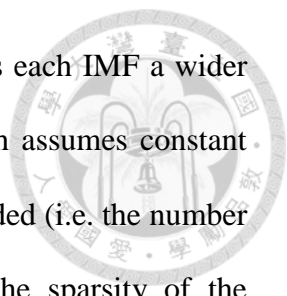
Empirical mode decomposition (EMD) [2] is an algorithm aiming to decompose a composite signal into intrinsic mode functions (IMFs). IMFs are oscillatory signals with separate spectral bands, each of which allows moderate time-varying frequency and amplitude modulations. By applying a series of iterations, the algorithm finds the “mode” of a signal from a high-frequency component, subtracts it, and finds another mode recursively. As a result, the signal is decomposed into a few intrinsic mode functions (IMF) and a residual noise, that is

$$s(t) = \sum_{k=1}^K s_k(t) \quad (1-1)$$

The distinctiveness of EMD lies in its non-parametric nature. In a process called “sifting,” the baseline calculated by averaging the upper/lower envelope is iteratively filtered out from the signal to reel off the high-frequency oscillation. This upper/lower envelope is determined solely on the extrema distribution of the signal itself and thus varies over time. The recently developed mathematical property of the sifting operator proved EMD to be a highly non-linear and non-stationary adaptive filter [1]: the time-varying extrema intervals determine the non-stationary frequency response. Nevertheless, before the theoretical foundation has built, researchers have found IMFs to be highly adaptive, and formulated the IMF into amplitude modulated-frequency modulated (AM-FM) signal, where

$$s_k(t) = A_k(t)\cos(\varphi_k(t)), \quad (1-2)$$

with $A_k, \varphi'_k(t) > 0 \forall t$.



Here, the frequency modulation is not constant; instead, it gives each IMF a wider range of frequency. Compared with Fourier or wavelet methods which assumes constant frequency ($\varphi'_k(t) = 0$), this representation reduces the components needed (i.e. the number of k) to reconstruct the original signal. The EMD thus ensures the sparsity of the decomposition.

Since its development, EMD inspired numerous approaches for the capture the philosophy of (2). In the original EMD and its modifications, the local extrema were adopted when finding the mode function; however, in other non-EMD-based methods, parametric basis functions such as a wavelet or Fourier function are first adopted for a frequency domain transform, and different criteria for mode separation are then applied. For example, the synchro-squeezed wavelet transform [3] aims at reallocating a time-frequency scalogram in pursuit of a well-separated intrinsic mode component. In empirical wavelet transform [4, 5], an adaptive wavelet filter bank is built on a pre-determined spectrum segment. In variational mode decomposition (VMD) [6], a separation of modes is applied on the Fourier spectrum, which is therefore stationary.

The distinctiveness of EMD lies in its nonparametric nature. In a process called “sifting,” the baseline calculated by averaging the upper/lower envelope is iteratively subtracted from the signal to extract the high-frequency oscillation. This upper/lower envelope is a cubic spline interpolation of the extrema, which are determined solely by the innate property the signal. The recently developed mathematical theories showed that this spline determines the nonstationary impulse response of the sifting operator, which makes EMD a highly nonlinear and nonstationary adaptive filter [1]. Nevertheless, since its development, EMD has shown outstanding capability for processing nonstationary signals

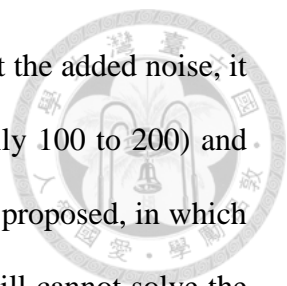
including speech [7, 8], coseismic accelerograms [9], and biological signals [10-12] as well as in the fault diagnosis of rotating machinery [13-16].



1.3.2 Modifications of EMD

Albeit powerful, there are occasions where the IMFs are difficult to be interpreted. One notorious problem is the intermittency, in which a signal with distinctive frequency (usually higher frequency) intrude for only a short period of time. In this case, the IMF is consisting of two different frequencies. This is a mode-mixing effect. Many modifications of EMD have been proposed to address the intermittency. Such modifications include two main directions. The first direction, which includes ensemble EMD (EEMD) [17], complementary EEMD (CEEMD) [18], Complete EEMD with adaptive noise (CEEMDAN) [19], masking EMD [20], and uniform-phase EMD (UPEMD) [21] involves the addition of an assisting signal so that the extrema are more evenly distributed.. The other direction involves adjustment of the knot position of the cubic spline [14, 22-25] or reconstruction of the undersampled extrema using a wavelet interpolation [5]. Both directions work well on intermittent signals characterized as single-tone oscillatory components. By increasing or adjusting the distribution of the extrema, these methods aim to equalize the extremum intervals of the entire signal; thus, the frequency response of the EMD is more consistent throughout different timeframes.

The most popular modification belongs to EEMD family. EEMD applies white Gaussian noise with amplitude dependent on the total power of the signal. The addition of white Gaussian noise solves the mode mixing by providing a full-band spectrum in all the time space, and EEMD behaves as a dyadic filter bank. However, two new shortcomings present, including residual noise due to the added noise and the mode-splitting effect in which



two or more IMFs contains components with similar scale. To cancel out the added noise, it requires to execute the algorithm under different randomizations (usually 100 to 200) and average the results. To boost the cancelation of added noise, CEEMD is proposed, in which the added noise comes in a pair (positive and negative one). CEEMD still cannot solve the mode-splitting problem, since the randomly generated Gaussian white noise put the same frequency component in the Nth IMF in some realizations but in the N+1th or N-1th IMF in other realizations. To solve this problem, CEEMDAN proposed to apply a pre-decomposed Gaussian white noise. In fact, this technique of applying a pre-filtered white noise, instead of a full-band noise, is similar to the masking-EMD which proposed at the same time as EEMD. Other EMD modifications which adaptively adds white noise also belongs to this kind.

In masking-EMD, a sinusoid with pre-determined frequency and amplitude is added. To cancel out the added frequency, the realization comes in a pair – positive and negative ones. The inconvenience lies the selection of the proper sinusoid. Rilling and Fladrin's [26] mathematical deduction gave us a hint to find the proper range with respect to the frequency and amplitude of our desired component under EMD. Ideally, if the sinusoid is properly chosen, there should be limited mode-splitting problem as compared to EEMD-related methods. However, there is still some residual noise problem in masking-EMD. The recently proposed UPEMD is a generalization of masking-EMD. In UPEMD, a set of sinusoid with the same amplitude and frequency but different phases are applied. It has been shown to be superior than masking EMD and CEEMD in suppressing residual noise and mode-splitting effect.



1.4 Spike problems

1.4.1 Spike problems in signal processing

Physically, a single spike may result from a single cause, such as the collective neuronal activity in EEG (Electroencephalography), or the electrical current surge caused by the switch. A spike has a very short time period but occupies a wide range within the frequency domain. Transforming of spikes in a time-frequency domain results in several to an infinite number of harmonics which mixed with real information. Therefore, for single-point spikes, the most widely adopted solution is the removal of spikes within the time domain, as is done by the median filter and its modifications [27-29]. For triangular spikes where the median filter cannot be used, a discrete wavelet transform is usually applied [30-32]. It would require choosing the appropriate wavelet functions similar to the spike shape, and decomposing the signal into different scales. The spikes can then be detected or removed in certain scales [30-32], and the new signal is reconstructed from the modified coefficients.

1.4.2 Spike problems in EMD

Decomposing spikes and steps of signals during EMD also results in spurious oscillations spreading throughout multiple IMFs. These spurious oscillations are similar to the harmonics of the spikes when decomposed through a Fourier and wavelet analysis. They only appear within a certain period of time in each IMF, acting as an intermittency signal [33]; as a result, they cause both mode-mixing and mode-splitting problems. Even though locality characteristic of EMD permits its effect to decay exponentially [1], the relatively strong magnitude of spike still results in perturbation of the IMF. Fig. 1-1 shows an example of Duffing wave with spikes decomposed by EMD. Compared to the IMFs from the same

Duffing wave without spikes, the ~ 0.1 Hz signal is split into IMF 1 and 2. This is called the mode-splitting effect. Granted that the above spike-removal methods can be used as preprocessing techniques before performing EMD, as seen in some applications [8], this frequency domain approach is inefficient and ineffective, and may lose its nonlinear and nonstationary property.

To the best of our knowledge, most EMD modifications that have been proposed to address the intermittency problem are not applicable to spikes or step functions. By increasing or adjusting the distribution of the extrema, these methods aim to equalize the extremum intervals of the entire signal; thus, the frequency response of the EMD is more consistent throughout different timeframes. However, because spikes occupy a very wide frequency spectrum, the unified frequency response in these modified EMD still decomposes a spike into several harmonics which intrude into the other components, as can be seen in Fig. 1-2. Therefore, a highly localized method focusing on adjusting only a few extrema is expected to solve the spike and step problems.

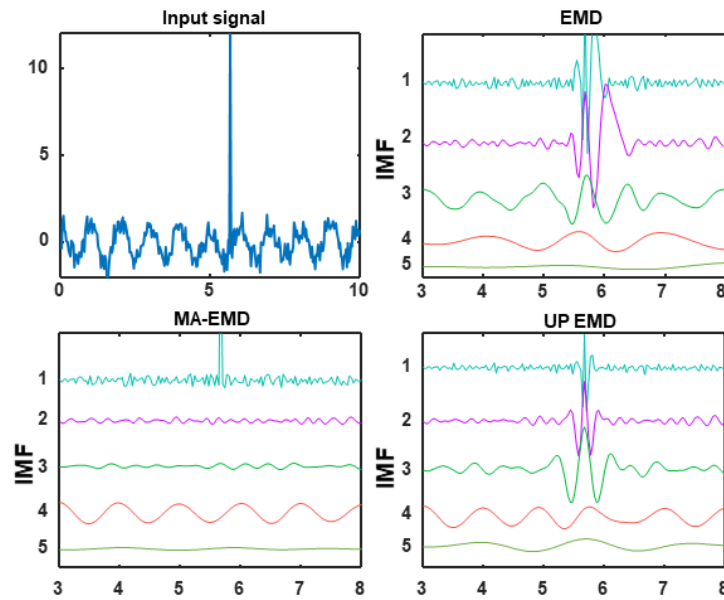
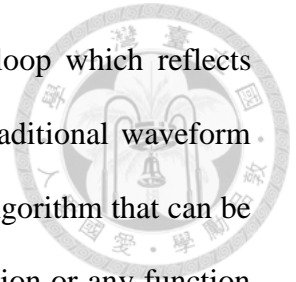


Figure 1- 2. Decomposing a sinusoid wave with a spike using different modifications of EMD (a) EEMD. (b) CEEMDAN. (c) UPEMD. (d) MA-EMD.

1.5 Overview

This dissertation consists 7 chapters. In this chapter, Chapter 1, we give a general introduction on the EMD and its related works, along with the spike problems in signal processing. In Chapter 2, we review the related theories and works related to our proposed work, including the EMD algorithm, its impulse response theory, the definition of the mode-splitting and mode-mixing, masking EMD algorithm, and the conventional spike detection algorithm which is applied to our MA-EMD algorithm. In Chapter 3, we make use of the mathematical representation of sifting to analyze the effect of a spike on the EMD, and propose our MA-EMD method that resolves the spike problem by isolating it in the first IMF. To further improve the extraction of spikes, masking aided MA-EMD (MAMA-EMD) methods are presented in Chapter 4. The validation of our method, limitations and some real-world examples are also provided. In Chapter 5, we apply our MAMA-EMD on a large database to detect potential atrial fibrillation (AF) patients by a standard 12-lead

electrocardiogram (ECG). This novel method analyzing the P-wave loop which reflects depolarization of atrial can better detects AF patients comparing to traditional waveform parameters from ECG delineators. In Chapter 6, we provide a general algorithm that can be used to apply our MA-EMD in the extraction of a Heaviside step function or any function whose Nth-order derivative is a spike. In Chapter 7, we state the conclusions of our study.



Chapter 2. Background



2.1 EMD

Given a signal $x(t)$ ($t > 0$), we define k as the IMF index and p the sifting step. Then, the notation $x^{k,p}$ represents the k_{th} proto-IMF at p_{th} sifting step. The EMD algorithm is given in **Algorithm 1**.

Algorithm 1: EMD algorithm

- (1) Define $x^{0,0} \triangleq x(t)$. Starting with $k = 1$ and $p = 0$. Set $x^{1,0}(t) = x(t)$.
 - (2) Identify all the maximum $\{(t_a, x_a)\}$ and minimum $\{(t_b, x_b)\}$ of $x^{k,p}(t)$.
 - (3) Connect maximum (respectively minimum) points with natural cubic spline to derive upper (lower) envelope $U(t)$ (and $L(t)$, respectively).
 - (4) Obtain the local mean of the upper and lower envelopes
 - (5) $m(t) = (U(t) + L(t))/2$.
 - (6) Subtract local mean from the temporal signal
 - (7) $x^{k,p+1}(t) = x^{k,p}(t) - m(t)$.
 - (8) Repeat (2)-(5) n_{sp} times, i.e. $p = 0, \dots, n_{sp} - 1$. Derive $x^{k,n_{sp}}(t)$.
 - (9) Assign the k_{th} IMF as $c_k(t) = x^{k,n_{sp}}(t)$.
 - (10) Calculate residual $x^{k+1,0} = x^{k,0}(t) - c_k(t)$.
 - (11) Increment k and repeat steps (2)-(8) to generate series of IMFs and a residue until that the residue contains no more than one extrema
-

2.2 Impulse response of EMD

In **Algorithm I**, steps (2)–(5) describe sifting, a process for subtracting the local mean from a signal. Here, we apply the analytical form of EMD derived by Wang et al. [1] to explain the effect of a spike on the sifting. In step (3), the upper/lower envelope is constructed

using natural cubic splines. Given the set of maxima points $\Gamma_x = \{(t_a, x_a), a = 1, 2, \dots, N\}$ where N is the number of maxima, the cubic spline of the upper envelope $U(t)$ is exclusively dependent on the positions and values of the maxima. Here, $U(t)$ can be written as the function

$$U(t; x(t)) = \mathcal{L}(\Gamma_x) \quad (2-1)$$

and satisfies the property of superposition [1, 34],

$$\mathcal{L}(\Gamma_x) = \sum_{a=1}^N x_a \mathcal{L}(\Gamma_a) \quad (2-2)$$

with input spline vectors $\Gamma_a = \{(t_j, \mathbf{e}_a), j = 1, \dots, N\}$ and scalars x_a . Notation \mathbf{e}_a indicates a unit vector whose only nonzero entry is at the a_{th} element. In other words, the upper envelope $U(t)$ is the summation of N different cubic splines sharing the same set of knot positions t_j and weighted by their individual maximum values x_a . The spline $\mathcal{L}(\Gamma_a)$ has the following two properties [11]:

- (1) It is a nonlinear time-variant impulse response of knot (t_a, x_a) to the other points.
- (2) It has a sinc-like curve satisfying the definition of a weak IMF, i.e., there is only one extremum between each pair of zero-crossing points, and the maxima and minima interlace with each other (Fig. 2-1(b)). Furthermore, because there is only one extremum between each pair of zero-crossing points, the cycle length (defined by the zero-crossing) of $\mathcal{L}(\Gamma_a)$ is the smallest extremum interval by at least two-fold. This is consistent with the frequency response derived by [26, 34], which states that when the interpolation points (which equal the extremum points) are equally spaced, the spline interpolator tends to be a low-pass filter with a cutoff frequency that is approximately half of the interpolating frequency.

Because the upper envelope $\mathcal{L}(\Gamma_a)$ is a low-pass filter, when the mean of the upper and lower envelope is subtracted, it becomes a high-pass filter. To summarize, the sifting process is equivalent to a high-pass filter whose frequency depends locally on the “grid size” of the sift, i.e., the knot interval, which is a result of the summation of different signal components [26]. Most of the modifications of EMD, either adding an assisting signal or adjusting the knot position of the spline, change the knot intervals and therefore the cutoff frequency of the filter.

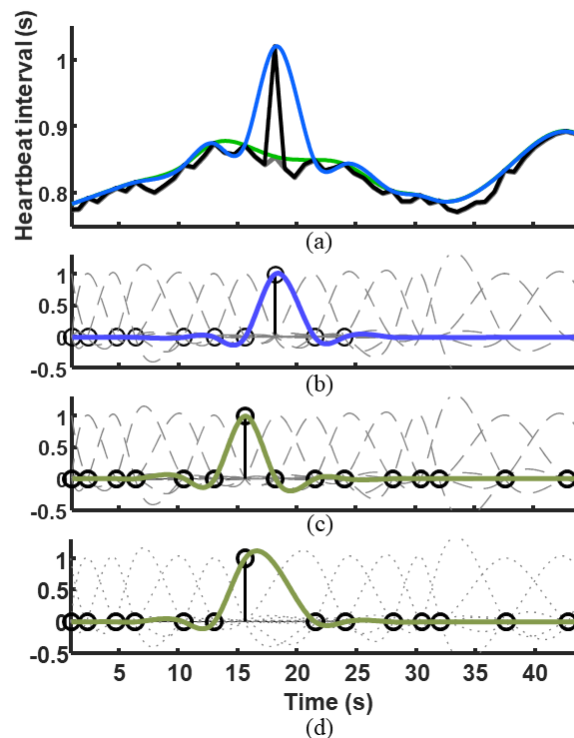
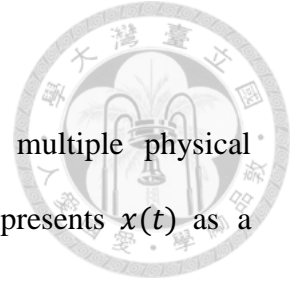


Figure 2- 1. The upper envelope, spline curves, and the effect of a spike.

(a) Series of heartbeat intervals $x(t)$ (gray) and the upper envelope $U(t)$ (green). One of the extrema is artificially changed to simulate an atopic beat. The new heartbeat series (black) has an upper envelope (blue) that is affected by the spike. (b, c) Spline curves $\mathcal{L}(\Gamma_a)$ for each maxima point (dashed line). The curves $\mathcal{L}(\Gamma_{a_s})$ generated by the spike (blue) and $\mathcal{L}(\Gamma_{a_{s-1}})$ generated by the neighboring point (green). (d) The spline curves $\mathcal{L}(\hat{\Gamma}_a)$ when excluding a spike point in the set of maxima (dotted line) and the new curve $\mathcal{L}(\hat{\Gamma}_{a_{s-1}})$ (green). Note that when a spike occurs, the shape of the envelope is similar to the spline curve and produces new extrema. When the spike point is directly skipped, the curve has wider knot intervals and a lower cutoff frequency.



2.3 Mode-mixing and mode-splitting

We consider a real-valued input signal $x(t)$ consisting of multiple physical components $s_k(t)$. The EMD algorithm shown in Algorithm 1 represents $x(t)$ as a combination of IMFs $c_m(t)$ and a residual $r(t)$:

$$x(t) = \sum_{m=1}^M c_m(t) + r(t). \quad (2-3)$$

The ideal result of a decomposition with IMFs $c_m(t)$ should be as follows:

$$c_m(t) \approx s_k(t), \quad (2-4)$$

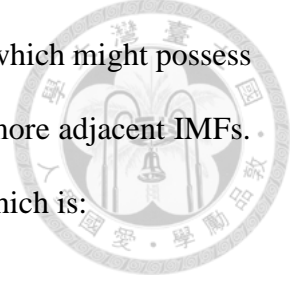
where each physical component should reside uniquely in a single IMF. The condition in which $c_m(t)$ contains two or more physical components is called mode-mixing [23, 33]; in contrast, when the amplitude of one $s_k(t)$ is split into two or more IMFs, mode-splitting occurs [17, 18]. In both mode-mixing and mode-splitting, the desired physical component is not sparsely represented and is either contaminated by or separated into other signals, thus encumbering further analysis.

One typical source of mode-mixing is the intermittency, where another signal with distinctive frequency is introduced for only a period of time. Noted that the frequency response of an IMF is dependent on the extrema interval, and the locally small extrema intervals results in a higher cutoff frequency during sifting. Therefore, the resultant IMF extracts the low-frequency components for most parts except the location with intermittency.

That is:

$$c_m(t) = s_k(t) + s_j(t), \quad (2-5)$$

for some $k \neq j$.



The mode-splitting is the effect that one oscillatory component, which might possess a physical meaning or have a narrow frequency band, occupies two or more adjacent IMFs.

Wang et al. [21] are the first to define mode-splitting mathematically, which is:

$$c_m(t) = \sum_{j=1}^{n_c} \alpha_{j,m} s_j(t) + \delta_m(t) \quad (2-6)$$

where $\alpha_{j,m}$ is the “attenuation ratio” representing the proportion of component j in IMF m with the equality $\sum_{m=1}^{n_{imf}} \alpha_{j,m} = 1$. In this representation, the mode-splitting effect is stationary. Indeed, the term “mode-splitting” is first mentioned by Huang and Wu [17] to denote the problem occurred in EEMD. When the same frequency component is resided in different IMFs in different realizations, taking average of all the realizations results in an energy splitting of the same component into different modes.

2.4 Masking EMD

Deering and Kaiser [20] proposed to insert a single tone sinusoid $w(t) = a_m \sin(2\pi f_m t)$ during the decomposition. This sinusoid, whose frequency is relatively higher, is a “masking signal” and serves as an assisted disturbance to avoid extraction of low frequency components during sifting. The algorithm is summarized in **Algorithm 2**.

Algorithm 2: Masking EMD algorithm

- (1) For step k in EMD, generate masking signal $w(t) = a_m \sin(2\pi f_m t)$.
 - (2) Perform Steps (2)-(5) in **Algorithm 1** on $x^+(t) = x^{k,p}(t) + w(t)$. In other words, substitute $x(t)$ by $x^+(t)$ to obtain IMF c_k^+ . Similarly, perform steps (2)-(5) in **Algorithm 1** on $x^-(t) = x^{k,p}(t) - w(t)$ and obtain c_k^- .
 - (3) The resultant IMF is defined as $c_k = (c_k^+ + c_k^-)/2$.
-

2.5 The spike detection

Mathematically, a signal with occasional artifacts can be modeled as

$$x(t) = \hat{x}(t) + v(t) \quad (2-7)$$

where $\hat{x}(t)$ is the signal of interest, $v(t)$ models the noise term and $x(t)$ is the observed signal. We suggest that the noise term contains two components

$$v(t) = \omega(t) + z(t) * i(t) \quad (2-8)$$

where $\omega(t)$ represents the white Gaussian process and $i(t)$ is the random process generating impulsive artifact which is convolved with a spike-like function $z(t)$. Here, $z(t)$ can be of different shapes, such as a single-point spike or a triangular spike.

Many types of impulse rejection filters have been designed for different types of signals, such as wavelet for speech signals [32] and Raman spectra [35], and median filters for images [29, 36]. We adopt one of the simplest designs, the median filter, as a tool for spike detection. Similar to other impulse detection algorithms, our spike detector is based on the prior assumption that the signal should be smooth. Therefore, the extrema that differ too much from nearby extrema is regarded as spike points. The maximum and minimum are dealt with separately. For each maximum $\{(t_{a_i}, x_{a_i})\}$, we first find the set containing D nearby maximum values (D is an even value) in a window centered about x_{a_i} .

$$W_i^D = \{x_{a_j} \mid i - D/2 \leq j \leq i + D/2\} \quad (2-9)$$

The median and standard deviation of this set are

$$m_i^D = \text{Med} \{x_{a_j} \mid x_{a_j} \in W_i^D\} \quad (2-10)$$

and



$$S_i^D = \text{std} \{x_{a_j} | x_{a_j} \in W_i^D\}, \quad (2-11)$$

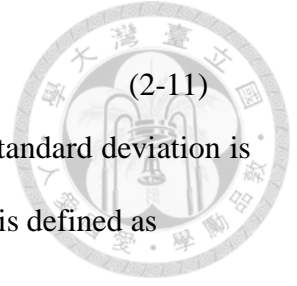
respectively. Then, the extrema values that are T times larger than the standard deviation is classified as maximum impulses, i.e. the set of maximum impulses, and is defined as

$$G^M = \{(t_{a_i}, x_{a_i}) | x_{a_i} > m_i^D + S_i^D \cdot T\} \quad (2-12)$$

Similarly, the set of minimum impulses is obtained as

$$G^N = \{(t_{b_s}, x_{b_s}) | x_{b_s} < m_i^D - S_i^D \cdot T\}, \quad (2-13)$$

where m_i^D and S_i^D are the median and the standard deviation of the minimum values within window W_i^D centered at x_{b_i} . Finally, we have the subsets G^M and G^N for the subsequent analysis.



Chapter 3. Effect analysis of spike in EMD and MA-EMD



3.1 Effect analysis of spike problem in EMD

Without loss of generality, we can formulate a spike as a shape function $z(t)$ at time t_0 (time shift):

$$x(t) = s(t) + z(t - t_0) \quad (3-1)$$

Supposing we have the spike resultant extremum (t_{a_s}, x_{a_s}) , the problem of a spike occurring during EMD has two aspects. First, the extremum itself might be additional to the original set of extrema, making the knot intervals half the original interval. Property (2-2) in the previous section states that the frequency response of a cubic spline is dependent on the knot intervals. That is, when a spike results in new extrema, the filter near t_{a_s} has a higher stop band than the other locations.

Second, because $x_{a_s} \gg x_{a_j}$ for some $j \neq s$, we have

$$U(t) = \mathcal{L}(\Gamma_x) = \sum_{a=1}^n x_a \mathcal{L}(\Gamma_a) \approx x_{a_s} \mathcal{L}(\Gamma_{a_s}) \quad (3-2)$$

That is, $U(t)$ is dominated by a single spline curve near the spike point; thus, the curve has a shape extremely similar to a sinc-like function (Fig. 2-1(b)). The upper envelope (and the local mean) are the results of artifacts rather than physically meaningful components. Furthermore, when the amplitude of a spike is sufficiently large, the shape of this cubic spline may generate additional knots during the iterations (see the simulation results in Sec. IV), making the inter-extrema interval even shorter than it should be.

When a spike introduces new extrema either by itself or by an amplified cubic spline, it results in locally shorter extrema intervals (i.e., a higher frequency curve) with respect to the other locations. The sifting of one component is interrupted in this area, leaving it to partially enter the next mode. Compared with the ideal results represented in Eq. (2-4), owing to the spike at time point t_{a_s} , $c_i(t)$ becomes

$$c_i(t) = \begin{cases} s_{i-1}(t), & \text{when } t \text{ close to } t_{a_s} \\ s_i(t), & \text{otherwise} \end{cases} \quad (3-3)$$

This is a mode-mixing problem in which $c_i(t)$ contains portions of both mode $s_{i-1}(t)$ and mode $s_i(t)$. Furthermore, mode $s_i(t)$ resides in $c_i(t)$ for most of t but splits into $c_k(t)$ for some $k > i$, resulting in a “mode-splitting” effect. Because this mode splitting only occurs during one period, it can be regarded as “nonstationary mode splitting.”

To show this, we experimentally generated two spikes on a Duffing wave (Fig. 3-1). The first spike is added to the position of the original extremum at $t = 28$; the second spike produces a new maximum at $t = 89$. Here, a Duffing wave is generated by numerically solving the following Duffing equation:

$$\ddot{x}(t) = x - x^3 + 0.1 \cos\left(\frac{2\pi t}{25}\right) \quad (3-4)$$

with the initial condition $x(0) = \dot{x}(0) = 1$. After the EMD operation, IMF $c_1(t)$ undergoes intermittent high-frequency oscillations near the second spike ($t \approx 60-70$), and a part of the 0.1-Hz component of IMF $c_1(t)$ moves into IMF $c_2(t)$. Comparatively, at the location near the first spike ($t \approx 15-25$), the signal frequency of IMF 1 determined by its relative cycle length is the same as in the original results; only the shape is distorted. IMF 2 also has the

same cycle length with a higher amplitude. This high amplitude results from energy leakage from the spike.

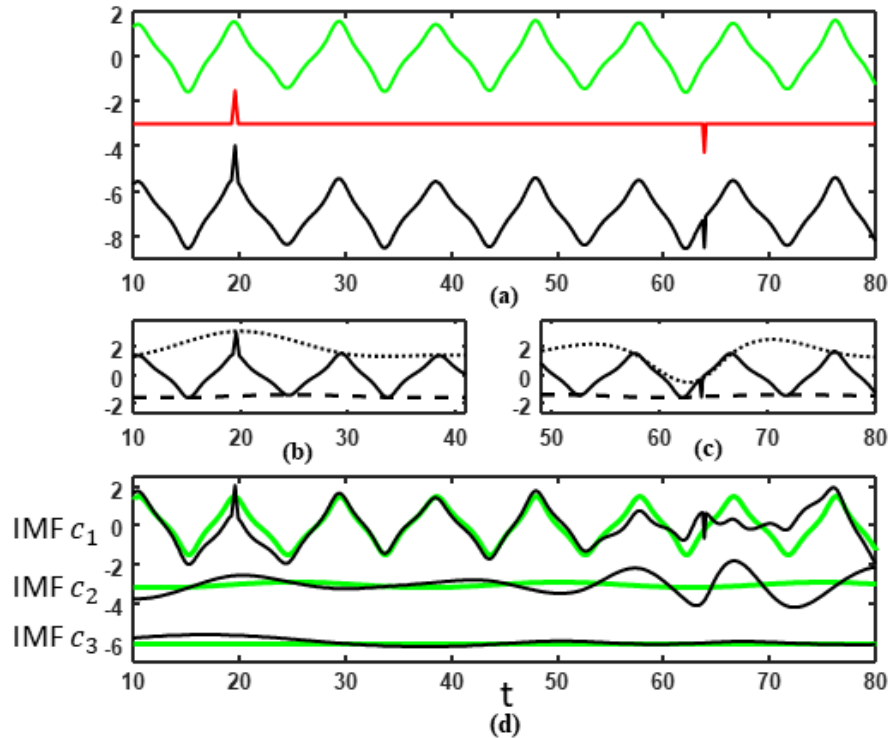


Figure 3- 1. The spike-interrupted Duffing wave and its decomposition by different methods. (a) The Duffing wave $S(t)$ (green), the triangle spikes $S_p(t)$ (red) and the summation of the two $x(t) = S(t) + S_p(t)$ (black). (b-c) The upper (dotted) and lower (dashed) envelope of the first sifting in EMD on $x(t)$ (solid). (d) The first 3 resultant IMFs (black) by original EMD on $x(t)$ and the IMFs (green) of the $S(t)$ as a comparison. IMF c_1 was split into c_2 near the location of the second spike which is not on the original extrema.

3.2 MSI: Measurement of mode-splitting

To quantify how extreme the mode-splitting is from S_i to IMF j , the mode splitting index (MSI) proposed. In our later simulations, we define the MSI as the amplitude of the frequency that S_i possesses within the Fourier spectrum of IMF j ; that is,



$$\text{MSI} = \sum_{f \in \omega} \frac{X_{c_j}(f)}{X_{S_i}(f)} \quad (3-5)$$

where $X_{c_j}(f)$ is the Fourier spectrum of IMF j and ω is the frequency range where the Fourier spectrum of S_i is larger than zero.

3.3 NE: Newly generated extrema

To validate our claim of newly generated extrema from spike and artifacts results in mode splitting, in our later simulations, we calculate the number of newly added extrema (NE) of the upper envelope in the first sifting when finding the first IMF as compared to the result with the upper envelope without a spike.

3.4 SK-EMD: skipping the extrema on spikes

To escape from the influence of spike, one trivial way is to directly skip it when calculating spline. we exclude those extrema on spikes from the set of knots and define the following:

$$\begin{aligned} \hat{\Gamma}_x &= \{(t_a, x_a), a = 1, \dots, N, a \neq a_s\} \\ &= \Gamma_x - \{(t_{a_s}, x_{a_s})\} \end{aligned} \quad (3-6)$$

and

$$\hat{U}(t) = \mathcal{L}(\hat{\Gamma}_x) = \sum_{a=1, a \neq a_s}^N x_a \mathcal{L}(\hat{\Gamma}_a). \quad (3-7)$$

This is efficient and guarantees that there is no impulse response from the spike during sifting. However, if the spike lies on the original spline point or covers the originally existing extrema, the knot interval becomes twice the original interval at this location (Fig. 2-1(c)). This lowers the frequency of the spline and may result in another mode-splitting problem in which mode



$s_i(t)$, with t close to t_a , is advanced to mode $c_{i-1}(t)$. In Sec 3.6, we will demonstrate this problem with a real example.

3.5 MA-EMD

3.5.1 Minimum arclength criterion

The alternative way is to keep all knot positions t_a but find a replacement \hat{x}_{a_s} for the spike point x_{a_s} in Eq. (3-2). In this study, we propose minimum arclength criterion to achieve this. Given a spike point (t_{a_s}, x_{a_s}) , we find a new (t_{a_s}, \hat{x}_{a_s}) such that

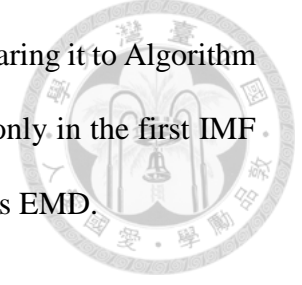
$$\hat{x}_{a_s} = \operatorname{argmin}_y \left\{ F \left(U(t|y_a = x_a, a \neq a_s; y_{a_s} = y) \right) \right\} \quad (3-8)$$

where

$$F(U(t|\cdot)) = \int_0^{t_N} \sqrt{1 + \left(\frac{dU(t|\cdot)}{dt} \right)^2} dt \quad (3-9)$$

is the arclength of $U(t|\cdot)$. Then, the modified spline is created by the new series of maxima with impulse point replaced by (t_{a_s}, \hat{x}_{a_s}) . Fig. 3-2 is an illustration of our proposed method. Here, the arclength is calculated over all the maxima points. However, this can be time consuming when the signal is long. In our experience, minimizing the arclength over 10 maxima points near the spike points is sufficient.

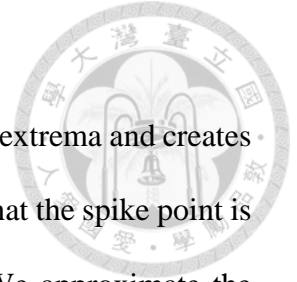
For all spike points in G^M , each point is processed consecutively. For the case of multipoint spike, the spike detection algorithm will mark two or more consecutive points on one single spike. (Here, we regard the whole structure as one single spike.) Minimizing the arclength point by point may not achieve the optimal result. The solution to this problem can be studied in future works.



The modified algorithm of EMD is shown as Algorithm 3. Comparing it to Algorithm 1, we added our protocol of detecting spike points and replacing them only in the first IMF (i.e. when $k = 1$). The rest of the IMFs are processed in the same way as EMD.

Algorithm 3: Spike extraction by EMD with minimum arclength method (MA-EMD) algorithm

- (1) Define $x^{0,0} \triangleq x(t)$. Starting with $k = 1$ and $p = 0$. Set $x^{1,0}(t) = x(t)$
 - (2) Identify all the maximum $\{(t_a, x_a)\}$ and minimum $\{(t_b, x_b)\}$ of $x^{k,0}(t)$
 - (3) If $k = 1$, find the subset of maximum impulses $G^M = \{(t_{a_i}, x_{a_i})\}$, $i = 1 \dots n_{spx}$, and also find the subset of minimum impulses $G^N = \{(t_{a_j}, x_{a_j})\}$, $j = 1 \dots n_{spn}$, where n_{spx} and n_{spn} are the total number of points regarded as maximum impulses and minimum impulses, respectively.
 - (4) Start with $i = 1$, find minimizer (t_{a_i}, \hat{x}_{a_i}) to minimize the arclength of upper envelope $U(t|x_a)$.
 - (5) Replace (t_{a_i}, x_{a_i}) with (t_{a_i}, \hat{x}_{a_i}) , and form the new set of maximum points (t_a, \hat{x}_a) .
 - (6) Repeat (4) and (5) for $i = 1 \dots n_{spx}$.
 - (7) For each $j = 1 \dots n_{spn}$, find minimizers (t_{b_j}, \hat{x}_{b_j}) to minimize the arclength of lower envelope $L(t|x_b)$, consecutively. Then, replace (t_{b_j}, x_{b_j}) with (t_{b_j}, \hat{x}_{b_j}) . Form the new set of minimum points $\{(t_b, \hat{x}_b)\}$
 - (8) Derive the new upper and lower envelope $U(t|\hat{x}_a)$ and $L(t|\hat{x}_b)$, respectively, according to the new set of maxima $\{(t_a, \hat{x}_a)\}$ and minima $\{(t_b, \hat{x}_b)\}$.
 - (9) Perform step (4)-(5) in **Algorithm 1**, which is to derive the local mean $m(t)$ and subtract it from the present signal to form the temporal signal
 - (10) $x^{1,p+1}(t) = x^{1,p}(t) - m(t)$
 - (11) Repeat (3)-(8) for $p = 0 \dots n_{sp} - 1$, and derive the first IMF, $c_1(t)$.
 - (12) For $k > 1$, the steps are the same as steps (2)-(9) in **Algorithm 1** of EMD.
-



3.5.2 Mathematical foundation

During the sifting process, a spike problematically produces new extrema and creates a local high-pass filter. With the minimum arclength criterion, suppose that the spike point is (t_s, x_s) and that its nearby extrema are (t_{s-1}, x_{s-1}) and (t_{s+1}, x_{s+1}) . We approximate the third-order polynomial curve using a first-order polynomial, i.e., a straight-line segment (Fig. 3-2). This generates a triangle $\Delta x_{s-1}x_sx_{s+1}$. According to geometry, the sum of the lengths of any two sides $\overline{x_{s-1}x_s} + \overline{x_sx_{s+1}}$ of a triangle is greater than the length of the third side $\overline{x_{s-1}x_{s+1}}$. Thus, if the minimum arclength $\overline{x_{s-1}x_{s+1}}$ is satisfied, we have no new extrema at x_s .

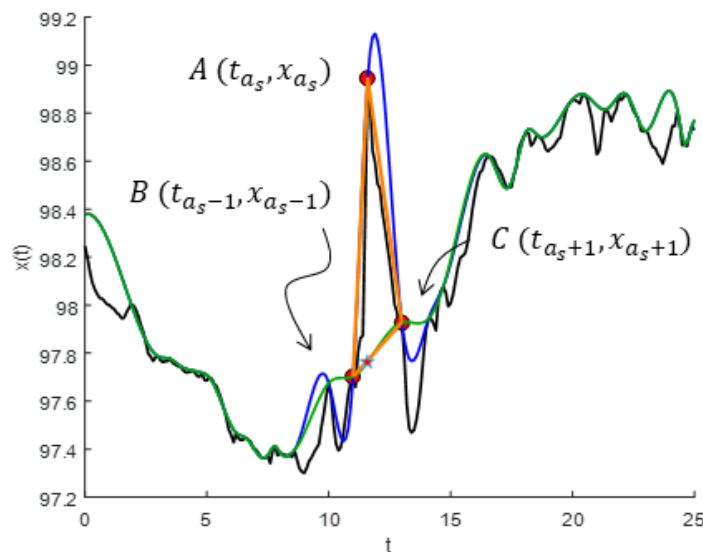
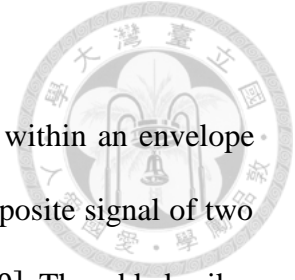


Figure 3- 2. Optimal replacement (pentagram) of spike point (A) found using the minimum arclength criterion.

The new envelope (green) has no new extrema at the spike position compared to the old envelope (blue). We approximate the cubic spline between points B-A and A-C by straight lines (orange). The triangular inequality guarantees that, under the minimum arclength criterion, there are no new extrema between B and C.



3.5.3 Simulation verification

We conducted two simulations to show the additional extrema within an envelope owing to the spike and their effect on mode splitting. The first is a composite signal of two pure sinusoids with $S_1 = 0.3 \cos(2\pi * 5t)$ and $S_2 = \cos(2\pi t)$, $t \in [0,10]$. The added spike, S_H , shifts from $t = 5$ to $t = 5.2$ and varies in height from 3 to 100 (Fig. 3-3). In each realization, we decompose the signal using a conventional EMD and our proposed MA-EMD (Figs. 3-4 and 3-5). In addition, we calculate the number of newly added extrema (NE) defined in Sec. 3.3. The mode splitting index (MSI) defined in Sec. 3.2 is then calculated as a measure of how extreme the mode-splitting is from S_2 to IMF 3. In our first example, the frequency of S_2 is 1; thus, $\omega = \{1\}$.

With the second simulation, we aim to decompose a signal composed of a randomly generated low-frequency signal S_L and a high-frequency sinusoid S_2 . A spike S_H is added to interfere with the decomposition. S_L is generated by filtering white noise with a 4–6 Hz bandpass filter; S_2 is again a sinusoid with an amplitude of 0.6 and a frequency of 15. In each randomization, we first generate S_2 and S_L . The spike S_H with height H is then added to the signal (Fig. 3-6). Decompositions by EMD and MA-EMD are applied on all $H \in [1,51]$ with an increment of 5. The NE of the upper envelope in the first sifting when finding the first IMF and the MSI for IMF 3 are also calculated for each decomposition. Here, ω for the MSI is set to 4–6 Hz. We applied 20 randomizations for each height. Finally, the NE and MSI for all randomizations with the same height were averaged. All the simulations are performed in Matlab 2018b. The program for MA-EMD is modified from the EEMD of Wu and Huang [17], and the program for EMD is from the latest version by Wang et al. [37].

The results are shown in Figs. 3-4 to 3-7. In both simulations, three findings were observed. First, the spike generated new extrema in the upper envelope in both the single-tone sinusoid and the randomly generated low-frequency signal. When the height of the spike is sufficiently large, NE is more than 1, i.e., more than the spike itself (Figs. 3-4 and 3-7). Second, the NE value generated is positively correlated with the height of the spike. Third, the MSI increases with an increase in NE. In addition, the MSI occasionally exceeds 1 by a large margin. This means that a spurious amplitude that does not exist in the original signal is created during the decomposition. In contrast, our MA-EMD generates no new extrema and therefore maintains a zero MSI.

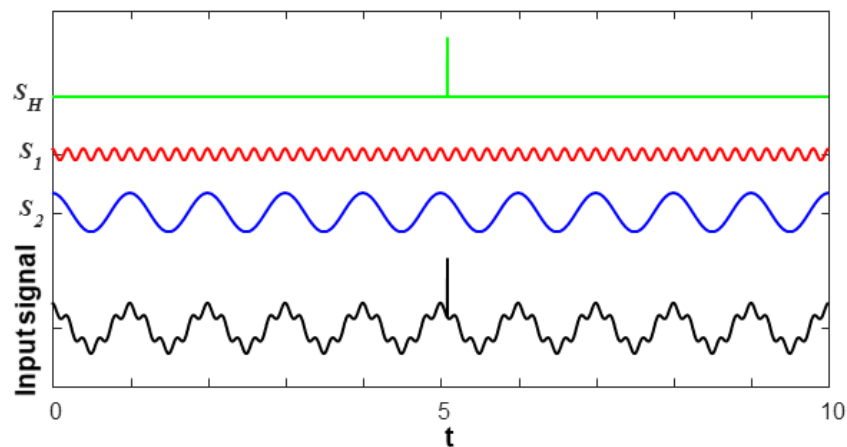


Figure 3- 3. Simulation 1: decomposing a two-tone signal with spikes of different heights and positions.

The figure shows one of the simulated spikes (S_H , green), the high-frequency pure sinusoids (S_1 , red), and the low-frequency sinusoid (S_2 , blue). The summation of S_H , S_1 , and S_2 is the input (black) for EMD and MA-EMD. In this example, the height of the spike is 3, and its position is at 5.08.

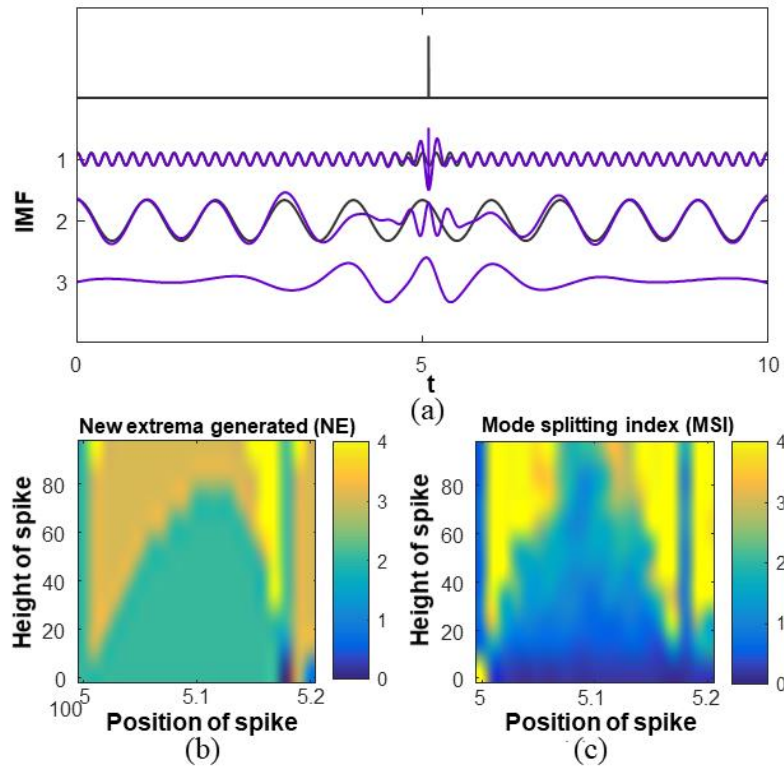


Figure 3- 4. The results of simulation 1 by EMD.

(a) The original signal (black) in Fig. 3-3 and the IMFs through EMD (purple). (b) The NE of the upper envelope in the first sifting when finding IMF 1. (c) The MSI of IMF 3.

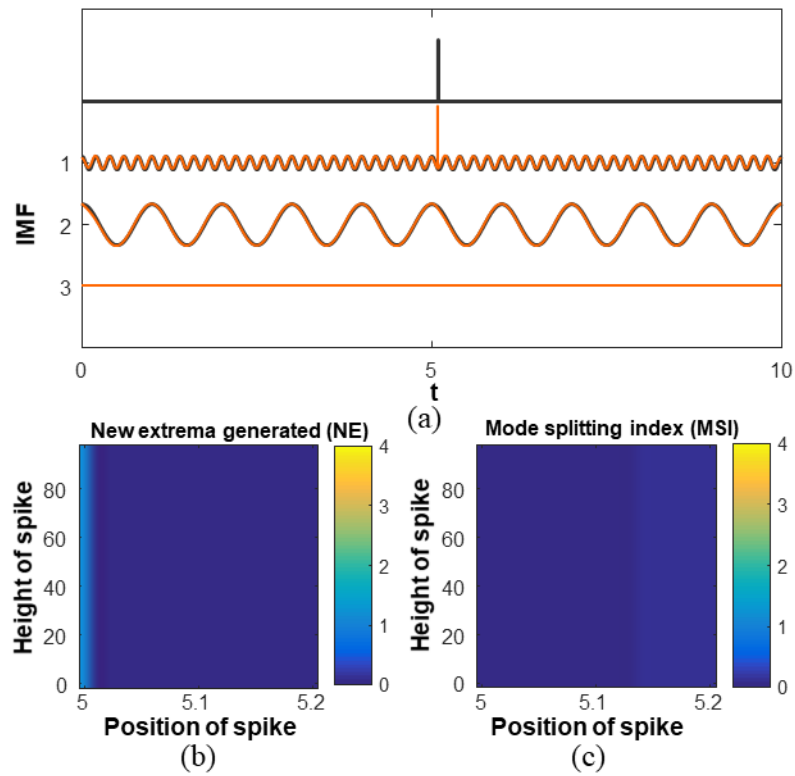


Figure 3- 5. The results of simulation 1 by MA-EMD.

(a) The original signal (black) in Fig. 3-3 and the IMFs through MA-EMD (orange). (b) The NE of the upper envelope in the first sifting when finding IMF 1. (c) The MSI of IMF 3.

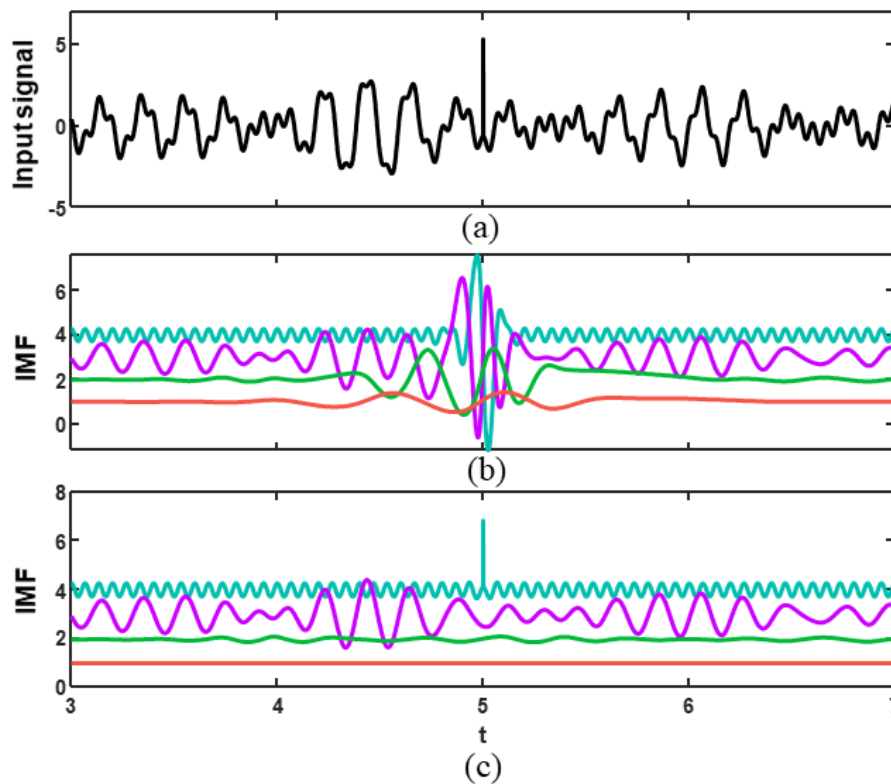


Figure 3- 6. Simulation 2: decomposing a randomly generated low-frequency signal with a high-frequency sinusoid and a spike of different heights.

(a) One of the simulations in which the height of the spike is 6. (b) IMFs derived by EMD. (c) IMFs derived by MA-EMD.

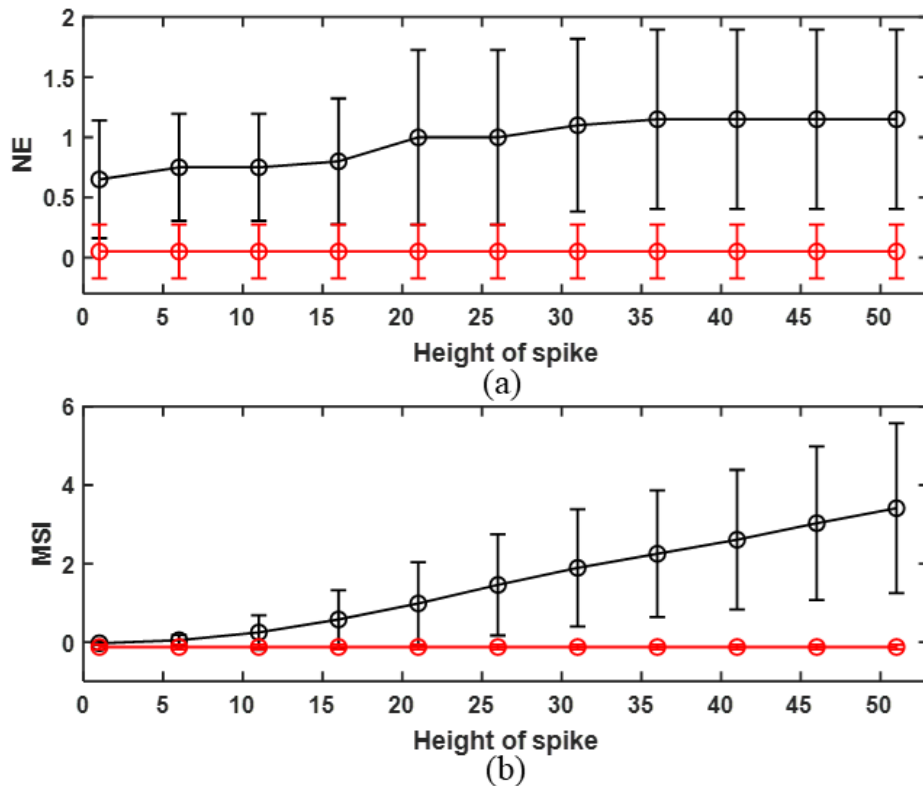
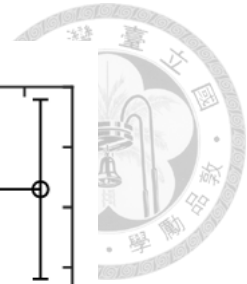
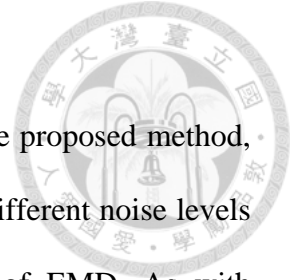


Figure 3- 7. The results of simulation 2 by EMD (black) and MA-EMD (red).
(a) NE of the upper envelope is calculated in the first sifting when finding IMF 1. (b) The MSI of the IMF 3. The circles represent the average values for 20 randomizations; the error bars represent the standard deviation.



3.5.4 Comparative accuracy analysis

To test the effect of background noise on the performance of the proposed method, we applied the decomposition of a sinusoid mixed with a spike under different noise levels and compared the results with those of a state-of-the-art variation of EMD. As with simulation 1 described in the previous subsection, the sinusoid is $S_L = \cos(2\pi t)$, $t \in [0,10]$. The spike is located at $t = 5.6$, and the height H is 3, 13, and 23 in different simulations. We added white Gaussian noise with varying signal-to-noise ratios (SNR) of $\{20, 15, 10, 5, 0, -5\}$ dB. The sampling frequency is 30. For each combination of the spike height and SNR, 100 randomizations were applied.

We chose to use multilevel uniform-phase EMD (UPEMD) [21] in the comparison because it has been shown to achieve a better performance than the other disturbance-assisted approaches in reducing the mode-splitting effects and residual noise effects. We chose eight phases and three levels. The frequencies of the perturbed sinusoids are 8.7, 4.3, and 2.1 for each level, and the amplitudes are all 1.4. For our MA-EMD, the masking frequency is set to 7 with amplitude = 0.4. After removing the spike from MA-EMD, the same UPEMD was applied to extract S_L . Traditional EMD was also applied on the same simulation as a comparison. In all three methods (EMD, UPEMD, and MA-EMD), the mode-splitting index (MSI), in which $\omega = \{1\}$, is calculated for IMF 5. In addition, the mean square error (MSE) of IMF 4, compared to the sinusoid, S_L , is calculated as a measurement of the reconstruction accuracy.

The results of our simulation are shown in Figs. 3-8 and 3-9. Note that the calculation of MA-EMD in Eq. 3-8 is the same for spikes of all heights because we have a single point spike with a very large slope. Thus, the results are the same for spikes of all heights. As

mentioned in the introduction, UPEMD acts similar to a high-pass filter for each IMF; thus, in the resultant IMFs, the spike is split into all of the IMFs. As a result, pure UPEMD is perturbed by a spike, resulting in a mode-splitting problem in which components with a frequency of 1 are present in both IMF 4 and IMF 5. When the spike is small, the performances of MA-EMD and UPEMD are similar. When the height of the spike increases, UPEMD results in larger MSI and MSE. Nevertheless, the original EMD performs the worst in the presence of the same spike heights and SNRs.

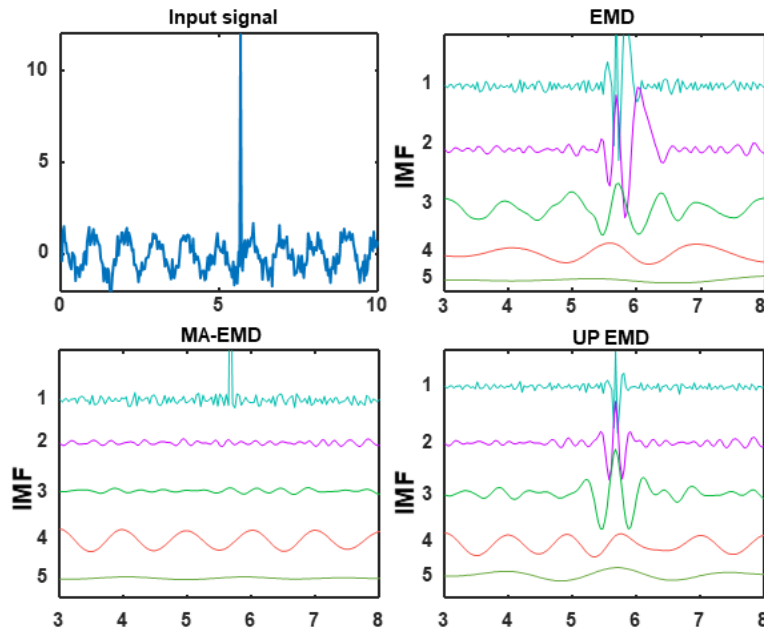


Figure 3- 8. Comparative accuracy analysis: decomposing a sinusoid with a spike under different SNRs using EMD, MA-EMD, and UPEMD. The SNR = 0 dB in this example.

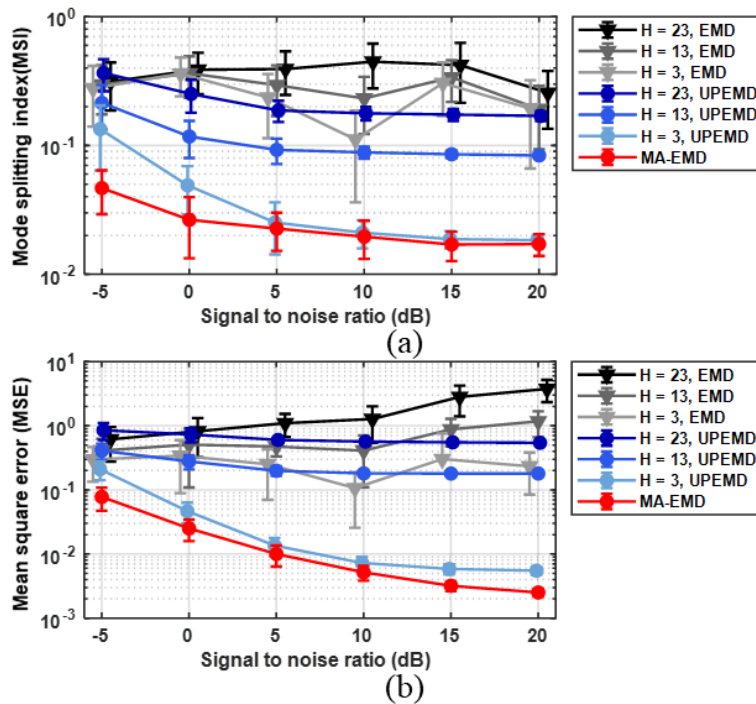


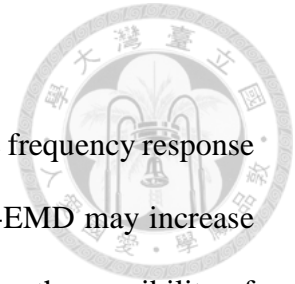
Figure 3- 9. The results of the comparative accuracy analysis.

(a) Mode splitting index (MSI) of the IMF 5. (b) Mean square error (MSE) of the IMF 4. The circles represent the average values for 100 randomizations, and the error bars represent the standard deviation. Note that the results of MA-EMD are independent of H.

3.6 Comparison between skip and MA-EMD

As discussed in Sec 3.4, SK-EMD is efficient but might lower the frequency response of the sifting due to reduced number of extrema. On the contrary, MA-EMD may increase the frequency response and is computationally more complex. Regarding the possibility of losing or adding new extrema, one possible policy to choose between the two methods is to compare the extrema interval at the spike point and the other locations. When losing the spike points as knots does not differentiate this knot interval from the average of knot intervals, SK-EMD may work well without problem of mode-splitting. Similarly, if skipping the spike makes the knot interval too large, MA-EMD can maintain the knot intervals in spline. This often occurs when the spike is of the shape of a triangle and masks the original extrema.

Fig. 3-10 demonstrates the mode-splitting problem in SK-EMD on the example of a set of core body temperature (CBT) data in which triangular spikes occur. The CBT data is from a thermistor probe in the anal sphincter, recorded every 6 minutes. We can observe the circadian rhythm in which a cycle length is around 1-day (Fig 3-10(a)). The triangular spikes are resulted from showering. In the analysis of circadian, we aim to extract the 1-day component in exactly one IMF. In conventional EMD, there is some mode-splitting effect on days 4 and 5, as can be seen in the time domain signal and spectrogram (Fig. 3-10(b) and (c)). On the contrary, when skipping these spike points, the 1-day component during this period advances to IMF 4 (Fig. 3-10(d) and (e)) due to the decreased extrema rate.



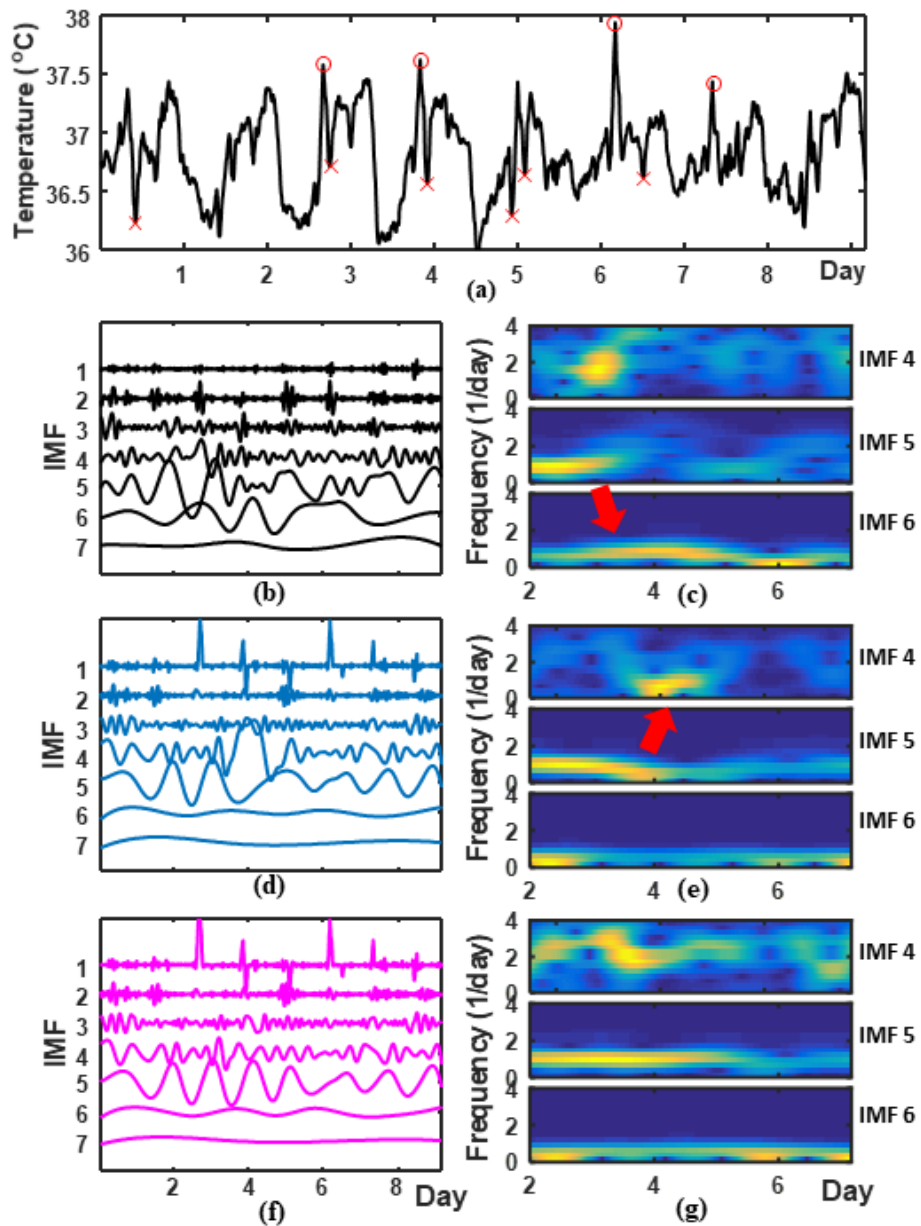


Figure 3- 10. The CBT data and the results from different methods.

(a) The CBT raw data (black) and the maxima (circle) and minimum (cross) defined as spikes. (b,d,f) The resultant IMFs of different decomposition methods. (c,e,g) The spectrogram of the IMFs. (b,c) EMD (d,e) skipping the extrema, and (f,g) MA-EMD. The red arrow indicates non-stationary mode splitting from IMF 5 to the previous (c) or later (e) IMFs.

Chapter 4. Masking-aided minimum arclength EMD

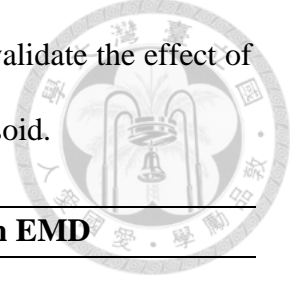


4.1 Introduction

The MA-EMD tracks the local mean without the influence of spikes. This indicates that the spikes are left in the first mode (IMF 1). However, if we want to separate the spikes from the first IMF, we propose the Masking-Aided MA-EMD (MAMA-EMD) [38]. The masking EMD [20] uses a pair of high-frequency sinusoids (positive and negative) in two separate EMD algorithms and then combines the results by averaging the IMFs. The idea is to insert a high frequency masking signal, the single sine tone $w(t)$, to the original signal to prevent lower frequency components from being included in this IMF. Then, perform sifting algorithm on $x^+(t) = x(t) + w(t)$, the resultant mode c^+ contains only spikes and the single sine wave. We repeat this algorithm on $x^-(t) = x(t) - w(t)$ and derive c^- . When averaging c^+ and c^- , the added masking signals were compensated. Thus, we have the new “first IMF” (IMF 0) that contains only spikes and some very-high-frequency components (most of time noises), leaving the IMF 1 free of spikes. The algorithm of our proposed masking-aided minimum arclength EMD (MAMA-EMD) is in **Algorithm 4**.

MAMA-EMD applies the MA-EMD in both masking algorithms. When the sinusoids are properly chosen, the spikes can be isolated in the previously non-existent IMF (IMF 0). Note that directly using the masking EMD can't separate the spike; instead, masking EMD serves as an adaptive filter that extracts only a high frequency components of the spike. The next section discusses how to find the appropriate amplitude a_M and frequency f_M for the

masking signal. A numerical simulation in Section 4.3 is performed to validate the effect of different a_M and f_M on separating a spike signal from a single tone sinusoid.



Algorithm 4: Spike extraction by masking aided minimum arclength EMD

- (1) Perform steps (1) – (3) in Algorithm 3 to detect spike points when $k=1$.
 - (2) Perform EMD to derive the first IMF. Analyze its peak-power frequency f_L and power a_L .
 - (3) Analyze the slope of each spike, choose the smallest, call it s_t
 - (4) Find the proper frequency a_M and amplitude f_M , such that they meet both (10) and (15).
 - (5) Generate masking signal $w(t) = a_M \sin(2\pi f_M t)$
 - (6) Perform steps (4)-(5) in Algorithm 3 on $x^+(t) = x(t) + w(t)$ to obtain IMF c_k^+ , and similarly on $x^-(t) = x(t) - w(t)$ and obtain c_k^-
 - (7) The resultant IMF is defined as $c_k = (c_k^+ + c_k^-)/2$.
 - (8) For $k>1$, the steps are the same as Algorithm 3.
-

4.2 Determination of masking signal

The inserted sinusoid should create no extrema on the spike, and allow EMD to separate itself from the original signal. According to Rilling and Flandrin [26], given two sinusoid $S_L(t) = a_L \cos(2\pi f_L t)$ and $S_M(t) = a_M \cos(2\pi f_M t)$, the necessary conditions to separate these two signals are

$$a_r f_r < 1 \text{ and } f_r < 2/3 \tag{4-1}$$

where

$$a_r = a_L/a_M \text{ and } f_r = f_L/f_M. \tag{4-2}$$

Similarly, there should be no extrema on the morphology of spike. For simplicity, we assume that the spike is a triangular-shaped signal ascending within the time range $[t_a, t_p]$ at

a slope s_t . In other words, the signal is $T(t) = s(t - t_a)$, when $t \in [t_a, t_p]$. Finding the extrema point is equivalent to solving the equation

$$\frac{d}{dt}[T(t) + S_M] = 0 \quad (4-3)$$

In other words,

$$\frac{dS_M}{dt} + \frac{dT}{dt} = 2\pi a_M f_M \cos(2\pi f_M t) + s = 0 \quad (4-4)$$

No extrema points means that the above equation has no solutions. Namely,

$$\cos(2\pi f_M t) = \frac{-s}{2\pi a_M f_M} \quad (4-5)$$

is not solvable. This leads to

$$\frac{s}{2\pi a_M f_M} > 1 \quad (4-6)$$

Thus,

$$2\pi a_M f_M < s. \quad (4-7)$$

The derivation above is based on an ideal situation where the signal to be separated is a pure sinusoid. In practice, we aim to use this method to separate spikes from the first IMF derived from EMD. Thus, the a_L and f_L can be the peak-power frequency and power of the first IMF. Therefore, to remove the effect of spike, we first detect the spikes and then find a proper masking frequency by analyzing the slope of the spike and the frequency of the first IMF from EMD to meet both Eqs. (4-1) and (4-7).



4.3 Simulation verification

4.3.1 Single Sinusoid

To validate our derivation of appropriate masking signals, we test the effect of different amplitude and frequency of masking signal in MAMA-EMD in extracting a spike from a single tone sinusoid. Without loss of generality, we set the frequency of the single-tone sinusoidal signal to be 1, since the filtering property of EMD is only related with the ratio of two frequencies, f_r , and amplitudes, a_r , of the pure sinusoidal signal and the added masking signal. The simulated signal and its components are $S(t) = S_L(t) + S_p(t)$, where

$$S_L(t) = \cos(2\pi t) \quad (4-8)$$

and

$$S_p(t) = \begin{cases} 200t - 380 & \text{if } 2 < t < 2.05 \\ -200t + 420 & \text{if } 2.05 < t < 2.1 \\ 0 & \text{otherwise} \end{cases} \quad (4-9)$$

Then, a masking signal $w(t) = a_M \sin(2\pi f_M t)$ is added to assist separating $S_L(t)$ and $S_p(t)$.

Next, we vary the masking amplitude a_M from 0.01 to 100, and frequency f_M from 0.95 to 20. The sampling frequency is 100Hz. Fig. 4-1 shows the time-domain waveforms of $S(t)$ and its two components. The result of separation is evaluated by the mean squared error (MSE) between the extracted IMF2 (sinusoidal) and $S_L(t)$.

Fig. 4-2 demonstrates the MSE of IMF2 versus f_M and a_M . As expected, the proper frequency and amplitude of masking signals is bounded by Eqs. (4-1) and (4-7). At the left hand side of the curve of $2\pi a_M f_M = s$, the spike is not separable from the $w(t)$. Meanwhile, at the right hand side of the curve, $a_r f_r = 1$ and $f_r < 2/3$, the masking signal is not separable from $S_L(t)$.

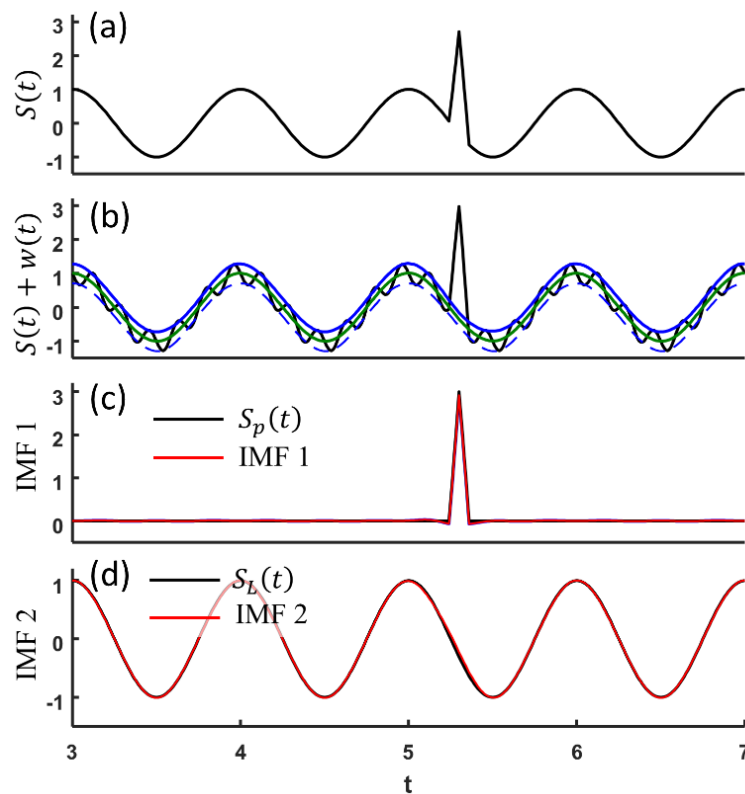


Figure 4- 1. The simulated signal and its decomposed IMFs.

The signal $S(t)$ is a combination of the triangular spike $S_p(t)$ (c, black line) and pure sinusoid $S_L(t)$ (d, black line). (b) A demonstration of summation of the signal and added masking sig (black solid line). The upper envelope (blue line) is connected by the adjusted extrema. The baseline (green line) is the average of the upper and lower (dashed blue line) envelop. (c) The triangular spike $S_p(t)$ (black line) and the first IMF from MAMA-EMD (red line). (d) The pure sinusoid $S_L(t)$ (black line) and the second IMF from MAMA-EMD (red line)

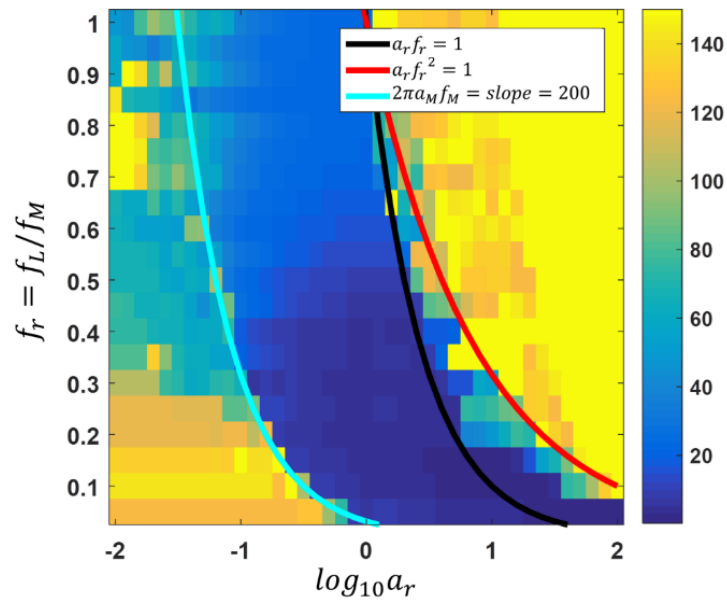
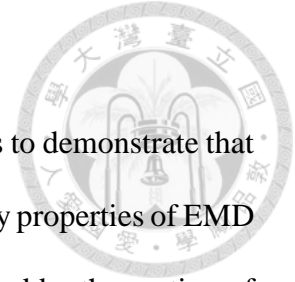


Figure 4- 2. The MSE of IMF2 extracted by MAMA-EMD for different f_M and a_M . The ground truth is a pure sinusoidal signal.



4.3.2 Duffing wave

We use nonstationary Duffing wave with artificially added spikes to demonstrate that the proposed method extracts, maintains the non-linear and non-stationary properties of EMD and suppresses the mode-splitting effect. Duffing wave can be understood by the motion of a pendulum with non-linear stiffness. The Duffing equation has the form in Eq. (3-4). We add three spike signals with slope 5, -8 and 10, and height 1.5, -1.3 and 2.9, respectively, and get spike-contaminated signals. The original Duffing wave, the spike signal as an artifact, and the spike-contaminated signal is shown in Fig. 4-2(a-c).

The IMFs from EMD by decomposing the Duffing wave serve as the ground truth of the decomposition. Three IMFs were derived from the decomposition (Fig. 4-3). The first IMF corresponds to the intrinsic frequency around 0.1 Hz which shows strong intra-wave frequency modulation structure; IMF 2 corresponds to a uniform intermediate frequency component representing the forcing function. The sub-harmonic term is the evidence for the non-linearity of the system. Moreover, its amplitude is very small, which means any error will destroy the waveform of the sub-harmonic motion; IMF 3 represents a very low-intensity sub-harmonics.

The decomposition results by EMD on the perturbed signal is shown in Fig. 4-3(d-f). Under the influence of spikes, the IMFs are disturbed, resulting in a mode-splitting effect, where the original 0.1 Hz signal is distributed in both IMF 1 and 2. Hilbert spectrum also shows the frequency shift from 0.1 Hz to three times larger in IMF 1 (Fig. 4-4(a)). The 0.1Hz during this period (80-100 sec) is split into IMF 2.

Then, we decompose the perturbed signal by the proposed method. Since the input signal itself is smooth and without noise, we use MAMA-EMD where a high frequency sine

wave is added in the first step to increase extrema points, so that the baseline, i.e. the signals except spike, can be depicted during sifting. The masking signal here has a frequency $f_M = 200$ and an amplitude $a_M = 3.5$. The result of our decomposition is depicted in Fig. 4-3 (g-j). In comparison to EMD, our MAMA-EMD method extracted the spike signal in the first mode, which is labeled as IMF 0 to avoid confusing with the original IMF 1. Afterwards, the later IMFs can be successfully recovered from the decomposition. Compared to the ground truth, our method only differs from the ground truth around both edges. The MAMA-EMD derived IMFs clearly depict the intra-wave frequency modulation in Hilbert spectrum (Fig. 4-4(b)).

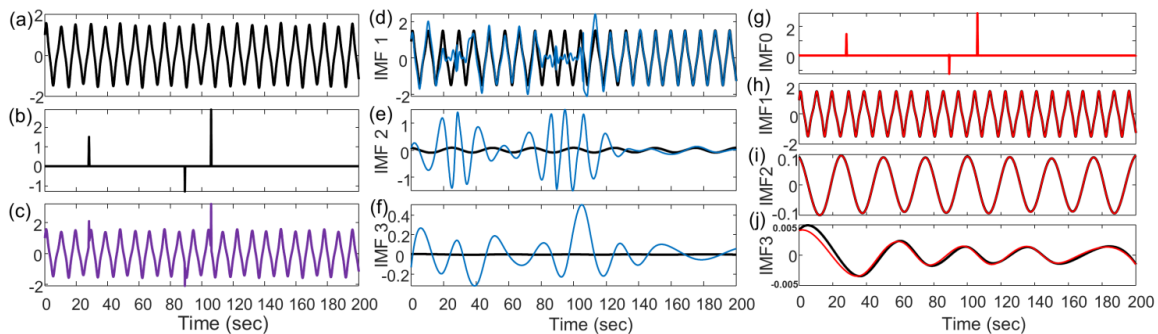


Figure 4- 3. Surrogated nonstationary Duffing signal contaminated by triangular spikes, and its decomposition by EMD and our proposed MAMA-EMD, respectively.

(a) Duffing wave. (b) The spike signal as a perturbation. (c) The spike-contaminated signal as the input for EMD and MAMA-EMD. (d-f) The blue lines are results of EMD on (c), and the black lines are from EMD on pure Duffing wave in (a) as the ground truth. (g-h) The red lines are MAMA-EMD on (c). The black lines in (h-j) are the same as the black lines in (d-f) but in different scales. Note that with MAMA-EMD method, the triangles are extracted, and the mode-splitting effect in (d-e), in which the 0.1Hz component in the first IMF of black line is split into IMF 1 and 2, is alleviated.

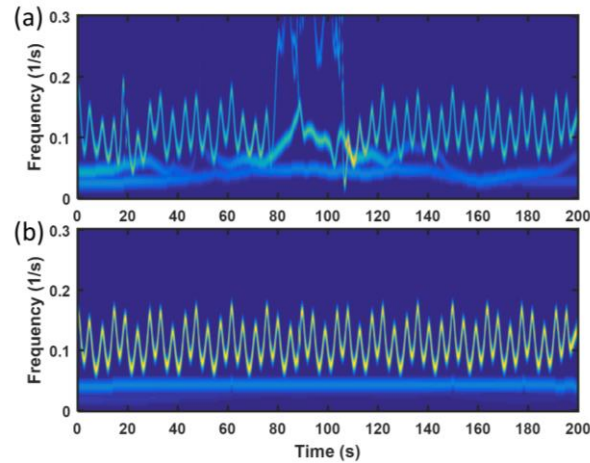


Figure 4- 4. Hilbert spectrum showing the frequency overlapping caused by spikes.
 (a) IMF 2-4 by EMD. (b) IMF 1-3 by MAMA-EMD.

4.4 Limitations

To use a masking signal, the frequency f_M and amplitude a_M of the added sinusoid $S_M(t) = a_M \cos(2\pi f_M t)$ must be determined. The criteria for choosing the frequency and amplitude of the added sinusoid were also proposed in Eqs. (4-1) and (4-7). However, there are some situations in which the spike is not separable from the first IMF even with the aid of a masking signal. The nature of EMD lies in the local means determined by the rate of the extrema [11], [42]. To separate the spike from the first IMF, the masking signal $S_M(t)$ should produce new extrema on the first IMF but not on the spike itself. Suppose the spike has slope s and that the peak-power frequency and power of the first IMF are a_L and f_L , respectively. This gives

$$a_L f_L / a_M f_M < 1 \text{ and } f_L / f_M < 2/3 \quad (4-10)$$

and

$$\frac{s}{2\pi a_M f_M} > 1. \quad (4-11)$$

Combining the above two inequalities, we have

$$s/2\pi > a_M f_M > a_L f_L. \quad (4-12)$$

When Eq. (4-12) does not hold, we cannot find a masking signal to separate the spike and the IMF; this implies the following:

$$s < 2\pi a_L f_L. \quad (4-13)$$

Note that this inequality implies that the background signal has extrema exposed on the spike. That is, if the spike is insufficiently sharp, we cannot separate it from the background even with the aid of masking signals.

4.5 Examples

4.5.1. Electrical current

Electrical current surge is a common problem in automatic control system. Conventional method of processing this signal is to use a linear low-pass filter, which does not remove the spikes effectively. Here, we demonstrate the performance of our proposed MAMA-EMD in solving this problem comparing to a Fourier-based low pass filter and traditional EMD.

The data were phase currents measured from three-phase AC servomotor (YBL-9D, Ye Li Electric & Machinery Co.,LTD) at 300rpm. The current values were transferred to voltage values by the current sensors. After filtered by RC low pass filter, the analogue voltage was converted to digital data by the microcontroller (STM32F103). A 3.3V 12-bit 1KS/s analog-to-digital converter was used.



The time domain signal and the Fourier spectrum are shown in Fig. 4-5(a,b). The spikes on the signals were caused by MOSFET switch on the three-phase inverter of the motor drive, and the frequency of switching was 10 KHz. The instantaneous switching would cause the current surges, resulting in the spikes on the signals. Furthermore, the microcontroller and the peripheral circuits would also generate high frequency noise. The phase current cycle represents the rotation of the engine. The harmonic (~40 Hz) in the Fourier spectrum showed that the signal is not pure sinusoidal.

First, the signal is filtered by a low-pass FIR filter with pass band equals to 15Hz. Fig. 4-5 (c) shows the results of filtering. Since a spike has a very wide band in Fourier spectrum, the designed filter can only decrease the height of spikes.

The decomposition result derived by EMD is shown in Fig. 4-6(a), where only the first 6 IMFs are given. The spikes even in the non-spike region disturb EMD, resulting in the mode splitting problem during the 0.2-0.4 second.

Then, the data is processed by our proposed MAMA-EMD. The spikes were first detected by the median filter described in Section 2.2 with window size 20 and threshold 1.5. The extrema detected as spikes are shown in Fig. 4-6(b, panel 1). Then, the first mode is derived from adding a masking signal with frequency $f_M = 200$ and amplitude $a_M = 3.5$. It can be observed that, our MAMA-EMD extracted the spikes and some high-frequency noise in the first IMF (Fig. 4-6 (b, panel 2)). The rest of the signal contains no spikes can be further processed by traditional linear filters or EMD. Here, we demonstrate the IMF 1-5 of decomposition results by EMD. In summary, it shows that our algorithm is capable of removing the spikes, and improves the decomposition of the rest modes.

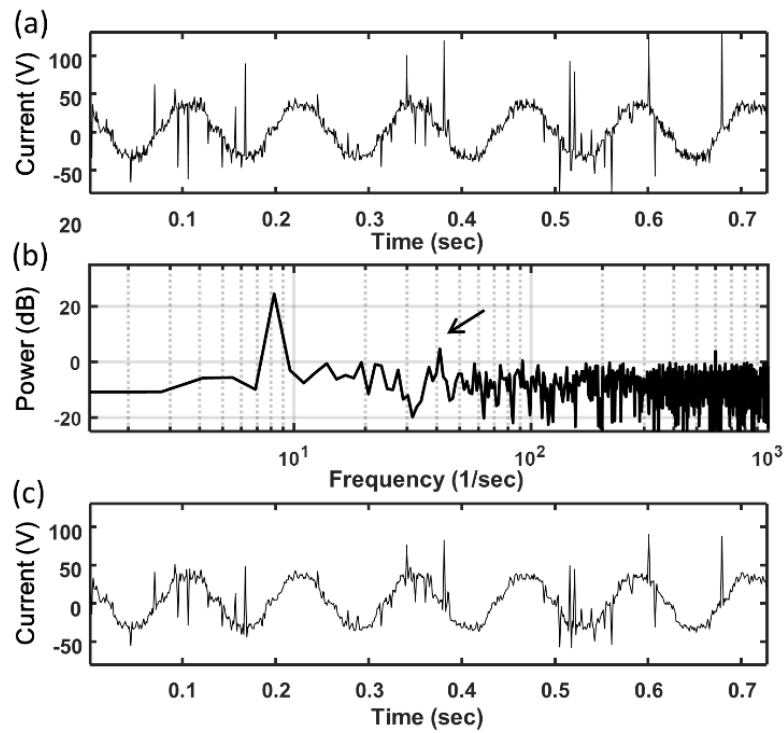


Figure 4- 5. Electrical current data.

(a) The time domain signal. (b) Frequency spectrum. The arrow indicates the harmonic at 40Hz. The spikes cannot be removed by a 15 Hz low-pass filter (c).

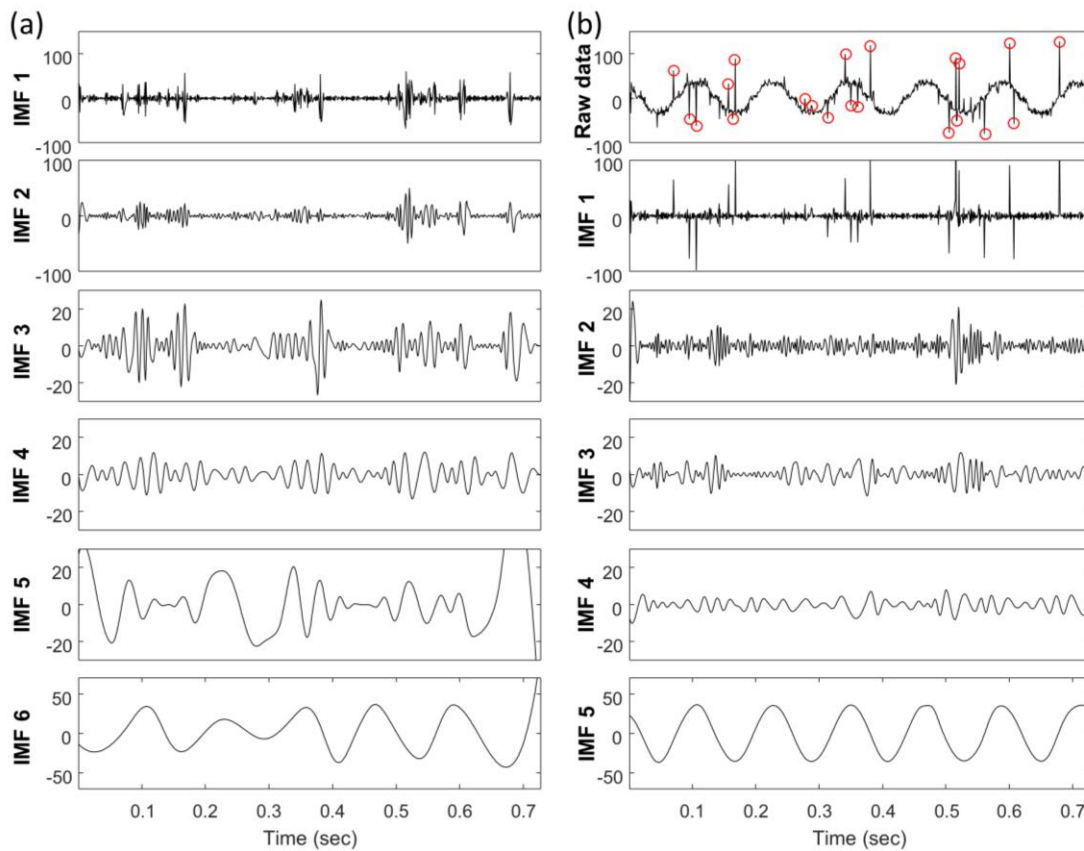


Figure 4- 6. Intrinsic mode functions of the electrical current data (IMFs) derived from EMD (a) and MAMA-EMD (b).

In (b), the first panel showed the original signal (black line) and the points detected as spikes (red circles). Panel 2-6 demonstrate the decomposition by our propose method. The first IMF contains the spikes and some high-frequency noise. The last panel shows IMF 5 that depicts the low frequency wave.

4.5.2 Rotor test rig

Vibration signals from rolling element bearing is adopted to verify our proposed method on realistic data. The faulty mechanical components often result in impulses-like vibration signals. These spikes, although including useful information, may cause mode mixing effects when decomposed by EMD. In fact, moderate de-noising before decomposition or filtering has been proposed to improve the fault detection algorithm [30,

39]. In the example demonstrated in this section, we show that our method can extract spikes in the first IMF and improve the accuracy of later analysis.

The experimental data are provided by Center on Intelligent Maintenance Systems (IMS), University of Cincinnati [40]. In this run-to-failure test, four Rexnord ZA-2115 double roll bearings were installed on one shaft. Each bearing was equipped with two PCB 353B33 High Sensitivity Quarts ICP® Accelerometers (x and y axis). Vibration data was collected for 1 second every 20 minutes for 164 hours with a sampling rate of 20 kHz, and the length of each data is 20480 points. The rotation speed is kept constant at 2000 rpm (rotation frequency $f_r = 33.3$ Hz), and a radial load of 6000 lb. was applied onto the shaft and bearings by a spring mechanism. At the end of the test-to-failure experiment, an inner race defect occurred on bearing 3. The inner race fault frequency f_i is 296.9 Hz.

Fig. 4-7(a) shows the time-domain waveform of the vibration signal. Note that our spike detection is defined on differences to extreme values of nearby extrema, not the absolute value of the spike point, and thus some of those seemingly large values are not detected as spike if its nearby extrema is also large (Fig. 4-7(b) and (c)). This provides an advantage to maintain the resonance excited by the impact of default.

The decomposition results derived by EMD and MAMA-EMD are shown in Fig. 4-8, where only the first 5 IMFs are presented. We performed envelop spectrum on IMF2 and 3. The envelop spectrum is the Fourier transform of the envelope of the signal. From the envelope spectrum derived from IMFs of both methods (Fig. 4-9), the inner race fault frequency ($f_i = 296.9$) and its modulation with rotation frequency (296.9 ± 33) can be found from IMF 2. However, our proposed method has a lower noise level and clearer peaks in both IMF 3, and clear peaks on the rotation-related frequencies $2f_r$ and $4f_r$.

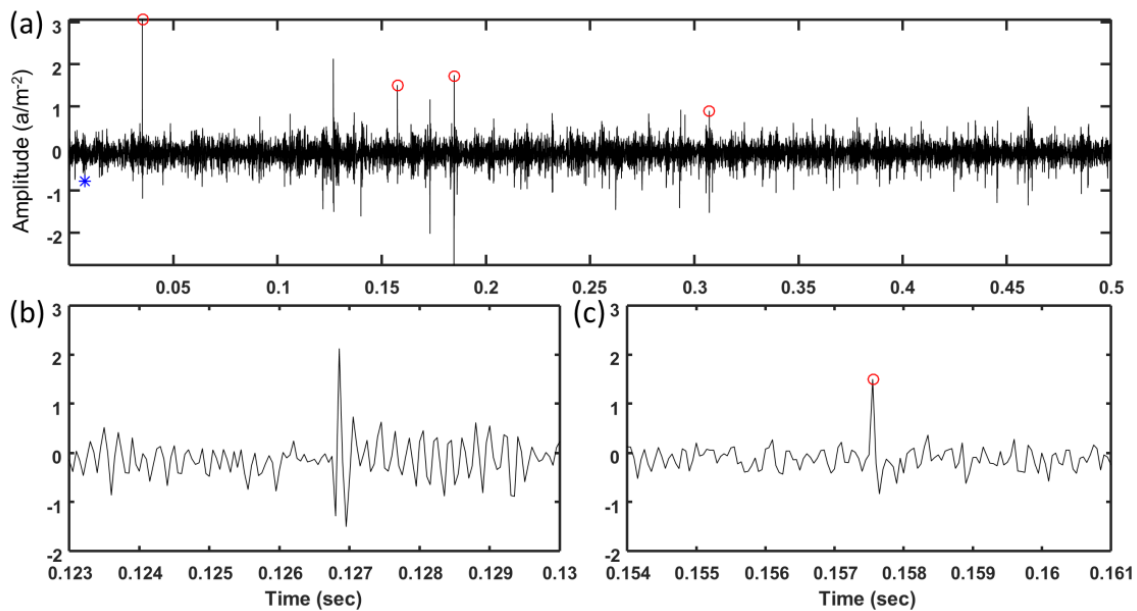


Figure 4- 7. A vibration signal from bearing 3 with inner race defect. Maxima spikes are denoted as red circles; minima spikes are blue stars. (a) The raw data. (b) and (c) are partial zoom-in of the signal.

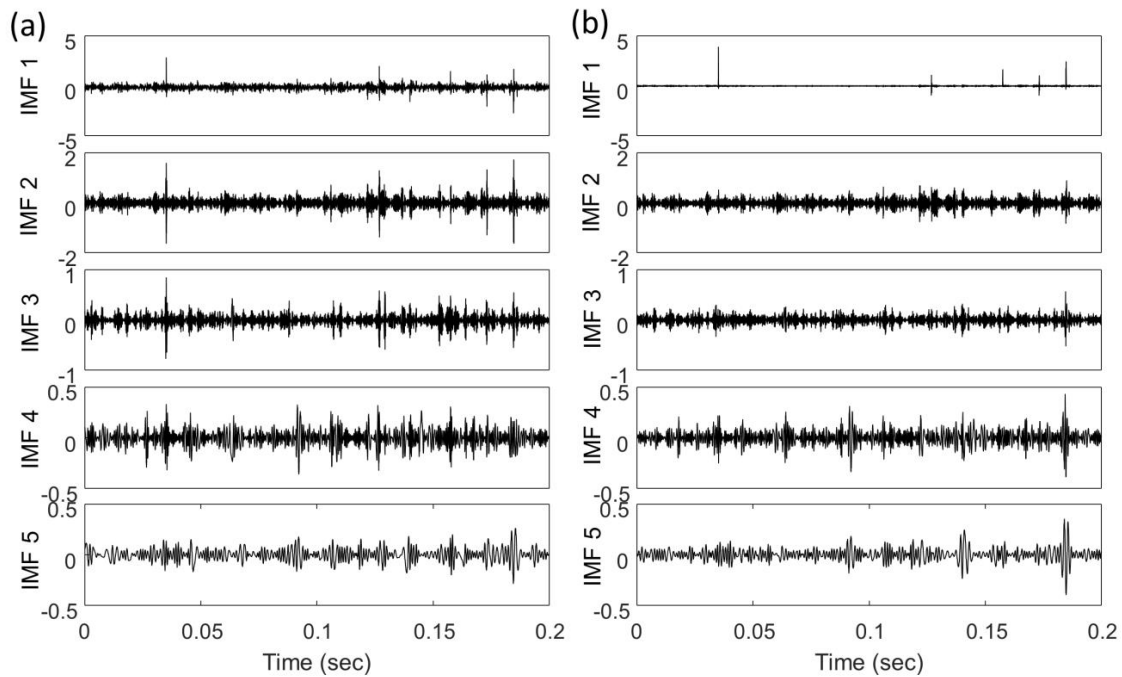


Figure 4- 8. Intrinsic mode functions (IMFs) derived from EMD (a) and MAMA-EMD (b).

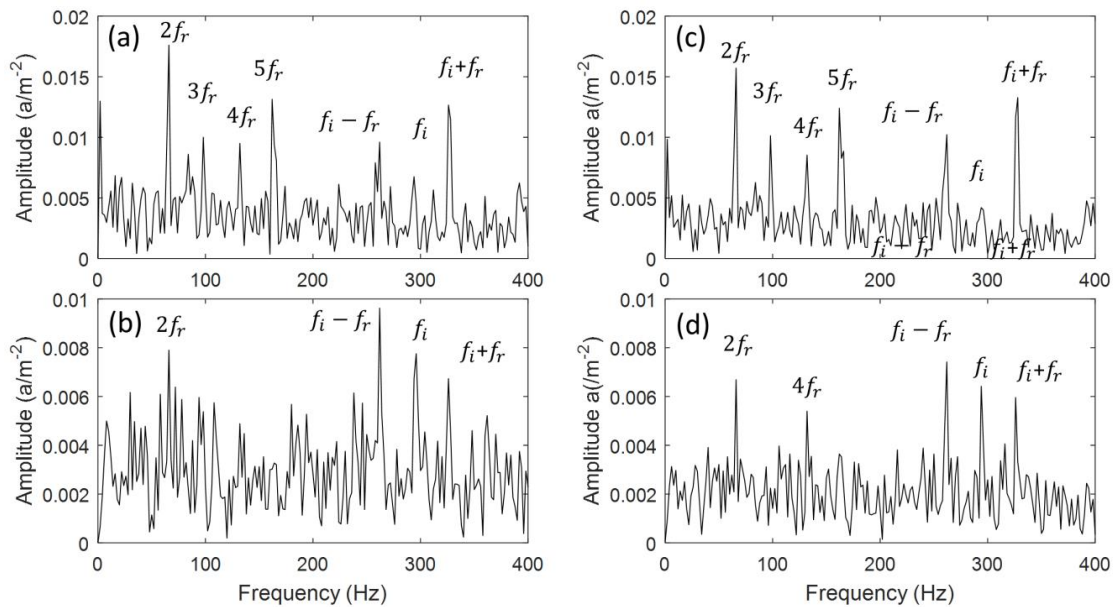
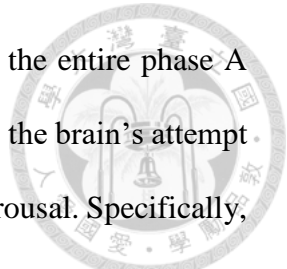


Figure 4- 9. Envelope spectra of components derived from EMD (a-b) and MAMA-EMD (c-d).

(a) and (c) are components from IMF 2; (b) and (d) are components from IMF 3.

4.5.3. Cyclic alternation pattern subtype classification in sleep electroencephalography

Neuronal signal often presents different shapes of spikes. In this section, we showed that the extracted spikes can be used as a feature preserving its physiological significance. The cyclic alternating pattern (CAP) is a periodic EEG (Electroencephalography) activity, which is characterized by sequences of transient electrocortical events that are distinct from background EEG activity. The CAP may signify sleep instability, sleep disturbance, or both [41]. CAP is composed of transitions between Phase A, identified by high-voltage slow waves, and the low-voltage irregular activity of at least 2 seconds (Phase B) (Fig. 4-10). Phase A activity can be classified into three subtypes based on the reciprocal proportion of high-voltage slow waves (EEG synchrony) and low-amplitude fast rhythms (EEG desynchrony) throughout the entire phase A duration. According to the standard, the



proportion of EEG desynchrony occupies <20%, 20-50% and >50% of the entire phase A duration in subtype A1, A2 and A3, respectively [42]. Subtype A1 marks the brain's attempt to preserve sleep; subtypes A2 and A3 often coincide with a frank EEG arousal. Specifically, 85% of subtypes A3 and 62% of subtypes A2 meet the AASM (American Academy of Sleep Medicine) criteria for arousals.

Here, we regard the high-voltage slow waves as spikes. By separating them from the background EEG, we can define the relative proportion of time between EEG synchrony and desynchrony and distinguish different phase A subtypes. The EEG is first processed by masking EMD to remove the first 4 IMFs which contain high frequency information (Fig. 4-11). The residual signal is then processed by MAMA-EMD to extract spikes. This extracted signal, called IMF 4_{sp}, which contains spikes is used to calculate proportion of EEG synchrony, defined as the proportion of time IMF 4_{sp} is above or below a threshold ($\pm 4\mu\text{V}$). We test our algorithm on the CAP Sleep Database [42, 43] (<https://physionet.org/pn6/capslpdb/#ref02>). This database includes polysomnography recordings, and the sleep microstructure is labeled by a team of trained neurologists. We use EEG recordings of the bipolar derivation C3-A2 from one of the normal subjects (n9) as an example. A total of 317 phase-A segments were analyzed.

Fig. 4-12 summarizes the result of our thresholding method on the three subtypes. The proportions of time with EEG synchrony are significantly different among the three subtypes ($P < 0.05$).

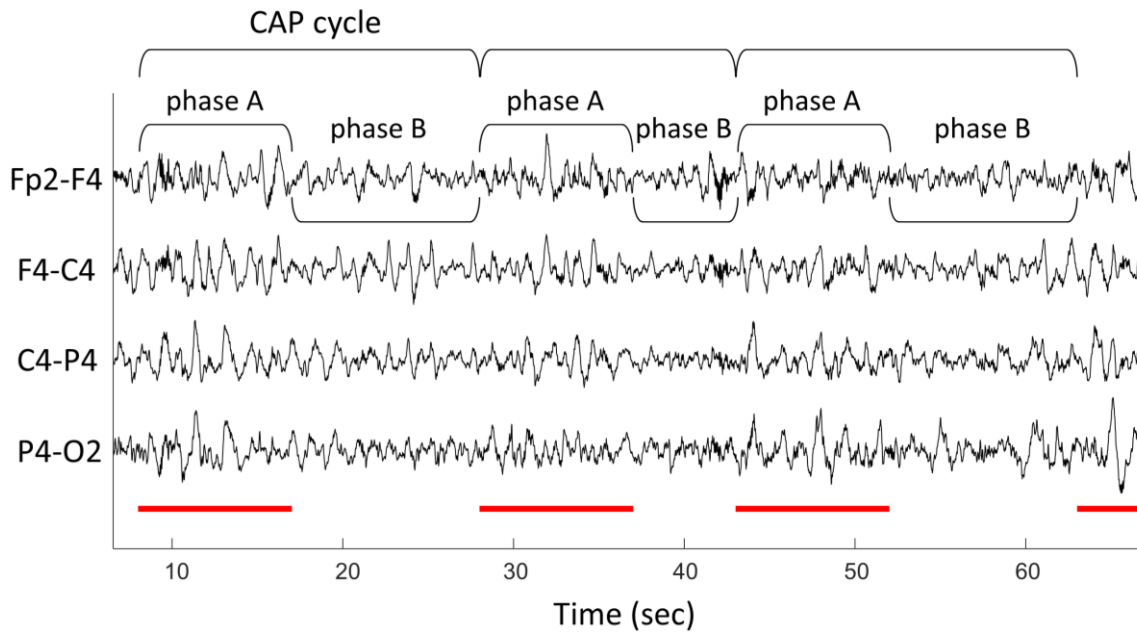


Figure 4- 10. An example of CAP cycles in 4 EEG channels (Fp2-F4, F4-C4, C4-P4 and P4-O2).

A CAP cycle is defined as a sequence of 2 alternating EEG patterns called phase A (indicated by red line) and phase B. Phase A is composed of high-amplitude EEG bursts which stand out from the background rhythm (phase B) in all the EEG channels.

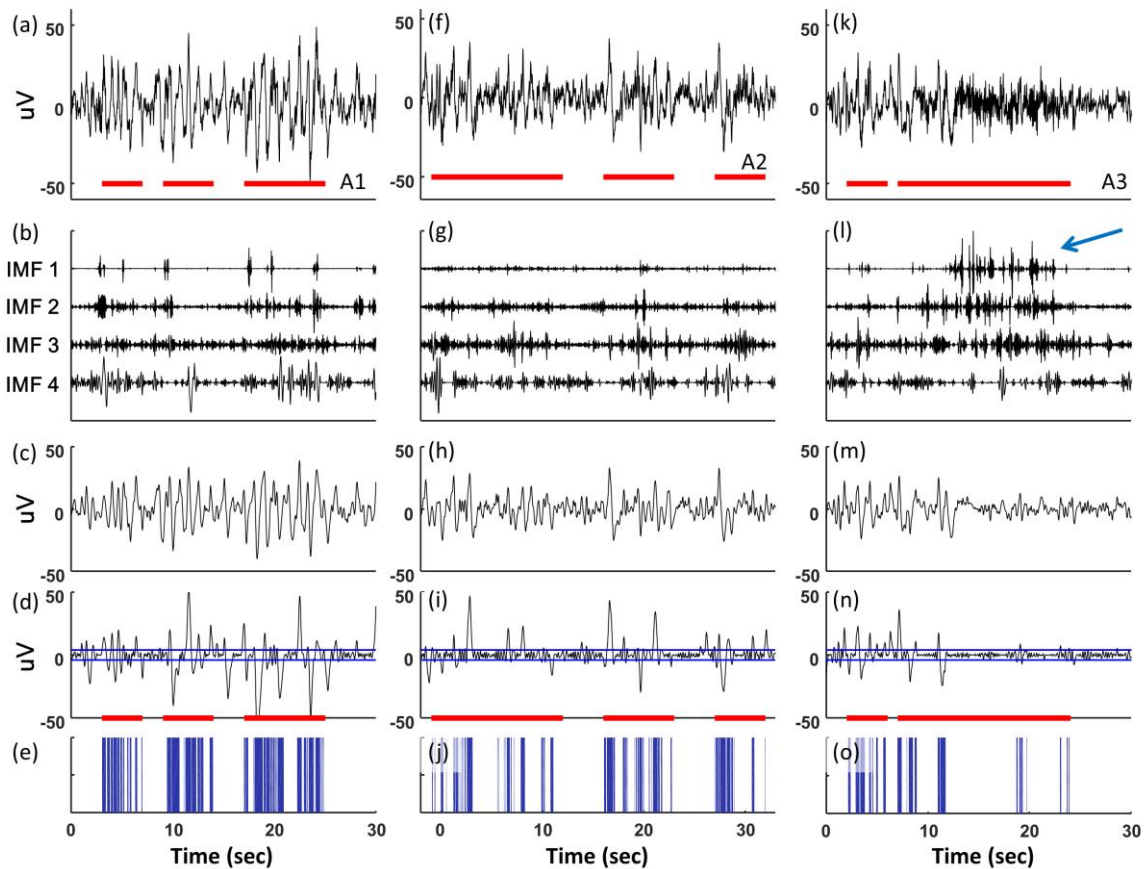


Figure 4- 11. An example of CAP cycles. A CAP cycle is defined as a sequence of 2 alternating EEG patterns called phase A (indicated by red line) and phase B.

Phase A is composed of high-amplitude EEG bursts which stand out from the background rhythm (phase B). Decomposition of the three different phase A subtypes, including subtype A1 (a-e), A2 (f-j) and A3 (k-o). The red horizontal lines indicate occurrences of A phase. The original signals (a,f,k) are first decomposed by masking EMD to remove the first 4 IMFs (b,g,i). The residual signals (c,h,m), derived by subtracting IMF1-4 from the original signal, are then processed by MAMA-EMD to extract the high-amplitude spikes (d,i,n). We then set up a threshold ($\pm 4\mu\text{V}$, blue lines in d,i,n) to identify whether the extracted spikes are above/under this threshold. The proportion of time that the spikes are above/under this threshold (indicated by blue areas in e,j,o) is distinguishable among different phase A subtypes. The blue arrow in IMF 1 of (l) indicates EEG arousal, which is often observed in subtype A3.

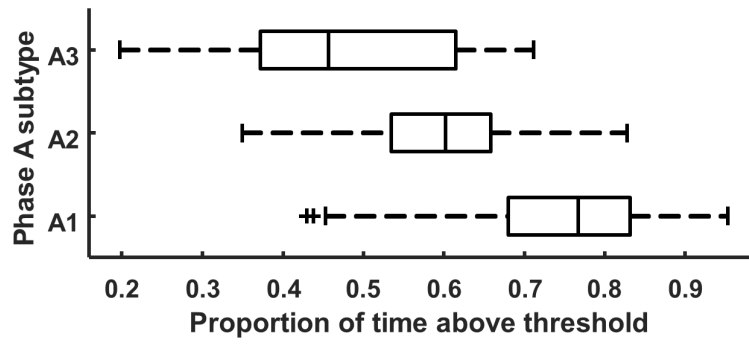


Figure 4- 12. Proportion of time that the extracted spikes in a phase A exceed the threshold.

Chapter 5. Application of MAMA-EMD on P-wave extraction for detection of potential atrial fibrillation patients

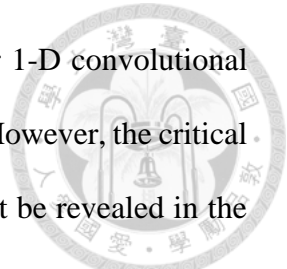


5.1 Significance for AF detection

Atrial fibrillation (AF) is a most common arrhythmia with an estimated prevalence of 1-4% in the general population [44]. Adults with AF are under a 5-fold greater of risk of stroke, 1.5-fold greater risk of all-cause mortality, increased risk of development and mortality of heart failure and higher risk of dementia [45]. Independent of other associated cardiovascular conditions, quality of life in AF patient is impaired [46]. The diagnosis of AF requires an electrocardiogram (ECG) documenting the typical AF rhythm. For potential patients with AF symptoms, general procedures in hospitals are usually an ECG Holter device which would be brought back home and used to record for 24-hr. Recent development of wearable devices with dry-electrode which enables patients to start recording only when symptoms occur [47] is another solution. However, for some AF patients, undiagnosed is common due to asymptomatic ('silent AF') and paroxysmal occurrence of AF [48]. Identify and determine potential AF patients under sinus rhythm during regular 12-lead ECG examination is crucial and beneficial for further prolonged systematic screening.

5.2 Recent works related to AF detection under sinus rhythm

There has been increasing evidence showing the structural changes in the atrial that develop atrial fibrillations [49], and these structural changes may reflect on the 12-lead ECG. Using 180922 patients with 649931 normal sinus rhythm ECGs, Attia et al. showed a 79%



accuracy in diagnosing AF patients under sinus rhythm with a 10-layer 1-D convolutional neuron network (CNN) on the eight physical leads in 12-lead ECG [50]. However, the critical features and clinical implications involved in the classification could not be revealed in the 1D CNN. The major challenges in identifying AF feature is the non-prominent P-waves in ECGs. Here in this study, we develop a method to isolate P-wave from ECG, and formulate P-wave related features which are free from interferences of QRS complexes. The aim of this study is to use feature based analysis to identify viable biomarkers for detecting AF patients under sinus rhythm.

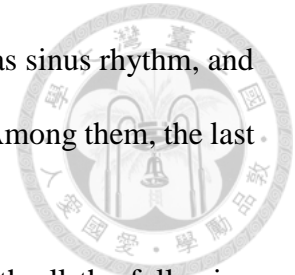
5.3 Method for P-wave analyses

5.3.1 Subject selection

We included all digital-available standard 10-second 12-lead ECG recordings from the Taipei Medical University Hospital between January, 29, 2015 and March, 07, 2020. A total of 94224 digital ECG recordings from 64196 patients were collected and de-identified. All ECG were recorded in the supine position by a trained physician at the sampling rate 500 Hz. All the recordings are diagnosed by trained cardiologists. The Taipei Medical University Hospital Review Board approved waiver of the requirement to obtain informed consent in accordance.

To select the recordings for identifying characteristic of potential atrial fibrillation during sinus rhythm, we first identified patients who are positive for atrial fibrillation by having at least one atrial fibrillation rhythm in these ECG recordings (Fig. 5-1). Many patients had multiple recordings over the inclusion period. To maintain the time dependence with atrial fibrillation instance, we defined a collection window of 90-days prior to the first

atrial fibrillation record. We consider only the ECG recordings marked as sinus rhythm, and 287 recordings from 213 subjects are selected according to these rules. Among them, the last ECG record diagnosed for each subject was included for the analysis.



The subjects for the control group were selected to comply with all the following criteria: (1) Each subject has at least 2 ECG recordings. (2) All the ECG recordings from the same subject are sinus rhythm. (3) Subjects have no ICA 10 codes of AF in their electronic medical records. A total of 3588 subjects meets the above criteria. Then, to avoid the effect of age on the ECG features, we use stratified sampling to ensure similar age distribution between AF and control groups. We set a 10-year age bin, and randomly sampled the subjects from each of the age groups between 50-70 to maintain the number of selected subject 2 times the AF group. The total number of selected control subjects are 247. After the subject list is determined, the first ECG recording for each subject were chosen in the analysis.

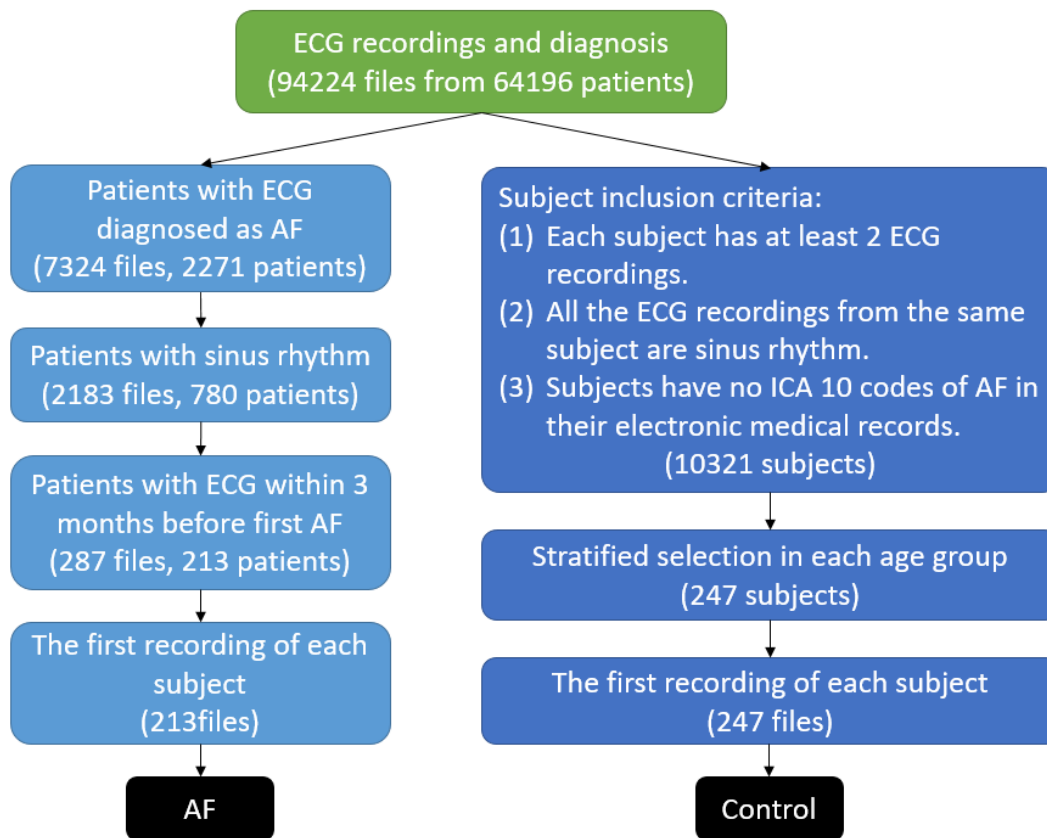


Figure 5- 1. Subject selection diagram.

5.3.2 ECG Signal processing

The scheme for this study comprises of signal processing, feature extraction and statistics. The complete flow chart of this study is in Fig. 5-2. Details for each step are given below.

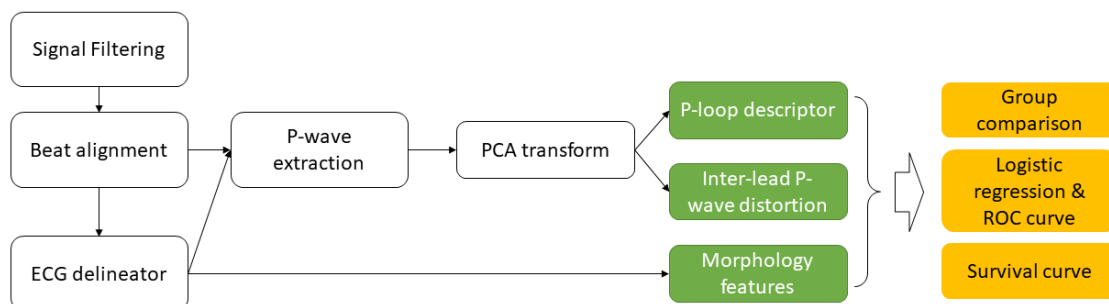
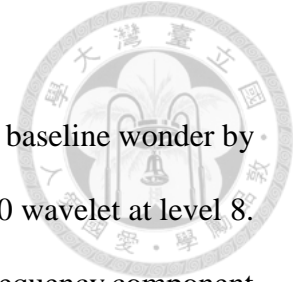


Figure 5- 2. Flowchart for the ECG processing and feature extraction for this study



5.3.2.1 Noise filtering

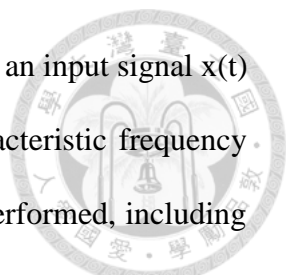
Electrocardiograms were resampled to 500 Hz. We first filter the baseline wonder by discrete wavelet decomposition. The ECG is decomposed with symlet 10 wavelet at level 8. The 8th approximate coefficient was set to zero to remove the very low frequency component. Then, the filtered signal was reconstructed using an inverse wavelet transform. Afterwards, a high pass filter with cutoff frequency equals to 32 Hz was applied. Some of the devices encountered artifacts in the first or last 0.5 sec and these artifacts were removed. Therefore, the length of the ECG recordings that are available for analysis ranges from 6.6-10.9 sec.

5.3.2.2 ECG Delineator

To identify the critical points on ECG for the later P-wave extraction and ECG morphology features, we used an open-source QRS detector and waveform limit locator, ECGPUWAVE [51], which has excellent performance for P-wave and QRS detector. Q-, R-, S-wave and the onset and offset of P-wave were identified for further processing.

5.3.2.3 P-wave extraction

The P-wave of an ECG reflects electrical activity originated from the atrial. Thus in this study, we aim at extracting features from P-wave. Our previously developed ECG features by the VCG and PCA will be largely influenced by the QRS wave and T wave which dominates ECG in amplitude and time, and thus we proposed a two-step algorithm to isolate P-wave from the ECG. The QRS wave was first removed by MA-UPEMD. Then, the baseline and T-wave of the QRS-removed ECG was delineated and subtracted by applying the MA-UPEMD again.



The EMD is an iterative algorithm which adaptively decomposes an input signal $x(t)$ into several IMFs. Each IMF is an oscillatory component with a characteristic frequency scale. In each iteration to derive an IMF, a series of sifting process is performed, including the following steps. (1) Identify local maxima and minima. (2) Calculate the upper/lower envelope by interpolating the local maxima/minima with a cubic spline. (3) Take the mean curve by averaging the upper and lower envelopes. (4) Subtract the mean curve from the signal. The steps (1)-(4) is repeated several times (usually 10) and the residual is an IMF. By subtracting the IMF from the $x(t)$ and repeating the sifting steps, several IMFs can be derived.

The MA-UPEMD is a combination of the two newly developed modification of EMD -- MA-EMD and UPEMD. With the MA-EMD, we aim at extracting spike functions of a signal in the first IMF. During each sifting for the first IMF, the height of extrema on the spike were adjusted to minimized the arclength of the cubic spline. This way, the spike is left with the residual after subtracting the mean curve. To remove the QRS-complexes, the Q-, R-, and S-waves are treated as spikes in MA-EMD. To improve the performance of QRS extraction and limit the range of cut-off frequency extracted by the MA-EMD, we further applied UPEMD, which has been shown to effectively suppress mode-splitting effect and residual noise problem. In UPEMD, a set of sinusoid signals of the same amplitude and frequency but with phases uniformly distributed within 2π was added into the input signal. The EMD is performed separately on each of the phases, and the IMFs from each realization is then averaged. The frequency of the sinusoid in the QRS extraction is 30 Hz and the amplitude is 0.02, and the number of phases is 4. The MA-UPEMD is to apply MA criterion on each of the realization of UPEMD, and the extracted QRS and the residual ECG which contains P- and T-wave are presented in Fig. 5-3 (b).

The remainder P- and T-wave still encountered serious baseline drift. Since we aim at preserving the intact waveform of P-wave, we did not use Fourier-based linear filters. We first take the averaged beat of each lead by aligning the beats with their original R peak position. Each subjects have a 1-sec by 12-lead ECG wave matrix. Then, the MA-UPEMD was performed on each lead of the average beat. This time, the P-wave was treated as spike, and the frequency of the added sinusoid is 10. The amplitude is 0.02 with 4 realizations. As a result, we have the isolated P-wave of the averaged beat for each of the 12 leads (Fig. 5-3(c)).

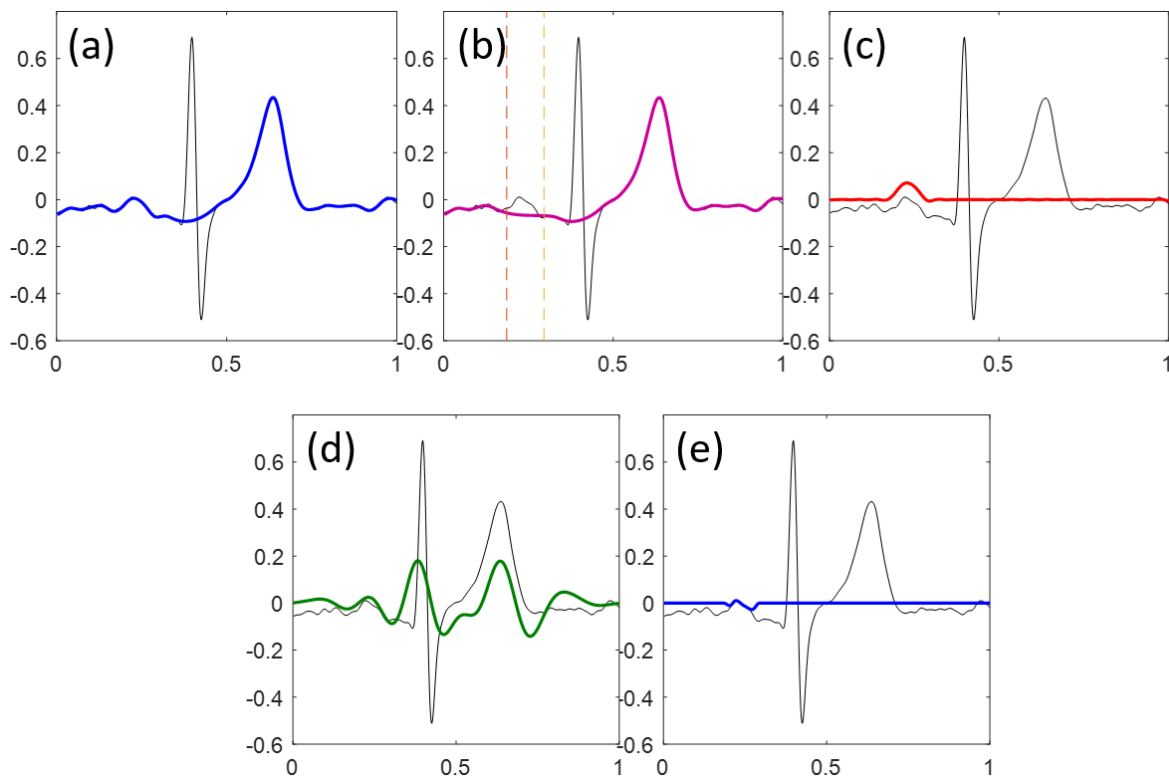


Figure 5- 3. The isolation of P-wave by applying twice the MA-EMD method. (a) The raw ECG (black) and the QRS removed signal (blue). (b) the delineated baseline wander and T-wave (purple). (c) The extracted P-wave (red), which is the subtraction of the blue line and purple line. The results by directly applying an 3-8 Hz bandpass IIR filter (Butterworth) and directly applying a Tukey window at the P-wave were also shown in (d) and (e), respectively, as comparisons.



5.3.3 Feature extraction

5.3.3.1 ECG morphology features

The conventional ECG morphological features were calculated from the ECG critical points detected by ECGPUWAVE. Due to collinearity, we chose the leads with the largest R amplitude among the limb leads and chest leads, respectively, and the morphological features were extracted on the averaged beat of the two chosen leads. The positions of ECG critical points include peak, onset, and offset of P-wave, onset and offset of QRS complex, Q-, R-, S-wave, and the peak, onset and offset of T-wave. The 3 types of ECG morphology features were defined bellow.

- (1) Wave amplitude. The amplitude of P, Q, S, and T wave is defined by the peak of the wave.
- (2) Duration. Traditionally features for ECG are calculated, including: the duration between P-onset and R-onset (PR interval), the duration between Q onset and J point (QRS duration), and the duration between Q onset and T offset (QT interval).
- (3) ST-voltage. The height of the ECG segment between J point and T onset, which is usually used for diagnosis of myocardial infarction, is also used. The average voltage between the two points were calculated.

5.3.3.2 Principle component analysis for P-wave projection

To analyze the depolarization route of the atrial, we map the 12-lead ECG to a 3D vector space spanned by the principle component (PC) of the ECG (Fig. 5-4). This transformation can better project the depolarization route to the x-y plane than the traditional vectorcardiogram transforms since each individual has a unique P-wave axis. This projection

method has been used on the QRS complex for distinguishing patients with arrhythmogenic right ventricular cardiomyopathy [52]. Here, we apply the same technique on the P-wave extracted ECG. We construct the P-wave matrix $X_{n \times 8}$ by 8 of the 12 leads (I, II, V1, V2, V3, V4, V5, and V6) with n observations ($n = 500$ points, 1 second), and decompose the correlation matrix ($X^T X$) by principle component analysis (PCA). The first 3 principle components U1, U2, and U3 occupy 99% of the total variance and is representative for the route and variation of the P-loop. The weighting of PC1, PC2, and PC3 (the eigenvalues) were included as a P-wave feature from PCA.

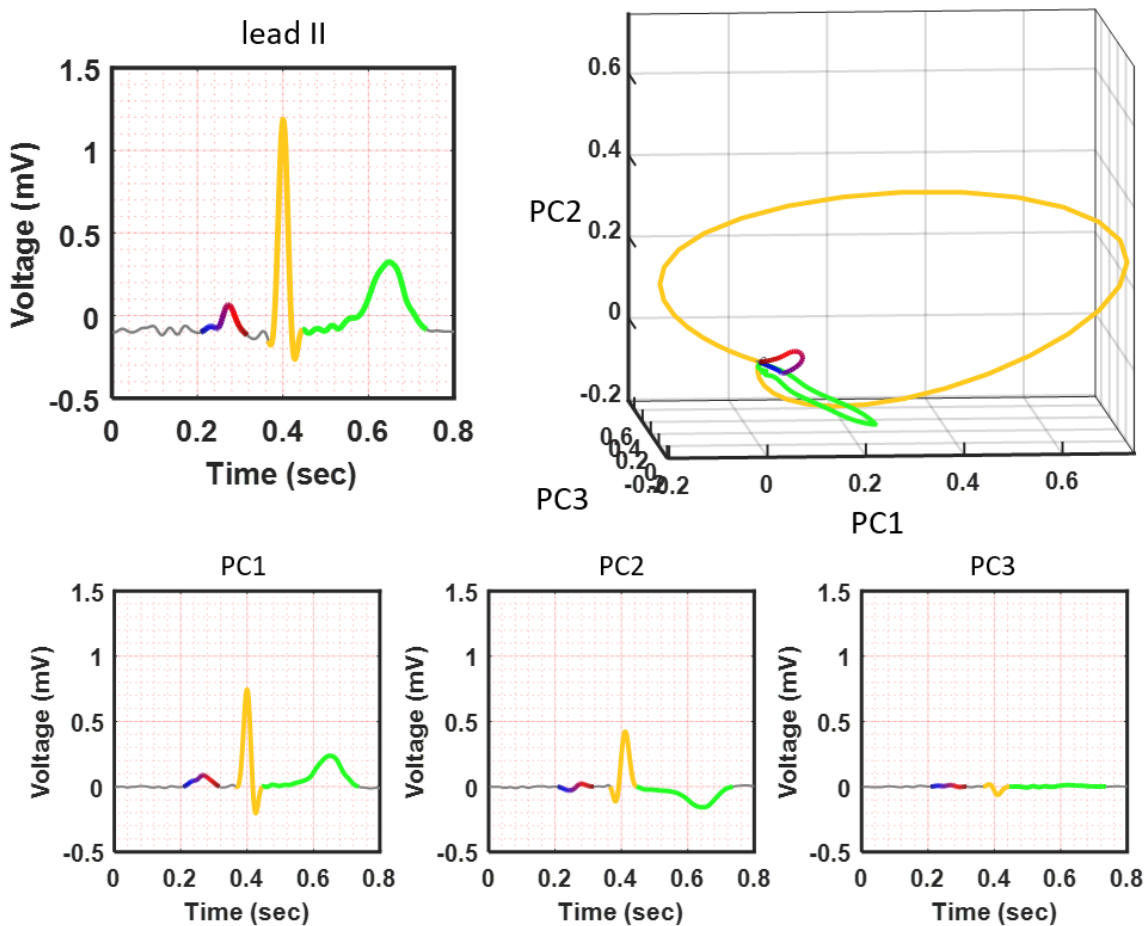


Figure 5- 4. The PCA transform for 8 of the 12 leads.

5.3.3.3 P-loop descriptors

Then, the previously developed QRS-loop descriptors [52] were applied on the P-loop. We calculated the area and length of the P-loop on the 2D plane expanded by PC1 and PC2 (Fig. 5-5). A minimum rectangle that encompasses the P-loop was divided into N cells (N = 4900 in this study) with equal size. The P-loop area (PA) is defined by the percentage of cells inside the P-loop. This area represents regularity of the loop and reduces when convex and concave components exist in this loop. The P-loop length is calculated by the total number of cells the route passes. The increase in P-loop length indicates the dispersion or inhomogeneity of the route.

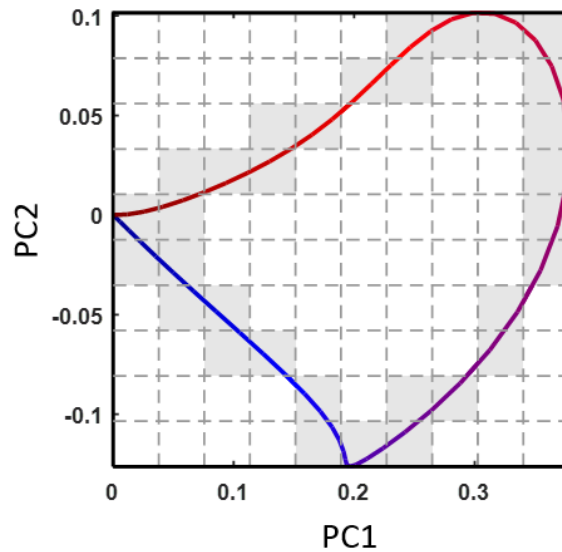


Figure 5- 5. The P-loop descriptor by PC1 and PC2.

The number of grey cells are the loop length, while the number of white cells inside the loop is the loop area.

5.3.3.4 Inter-lead P-wave dispersion

We further measured the dissimilarity of the P-loop between potential AF patients and normal subjects by analyzing the inter-lead relationships. This was previous used on the

QRS loop and was named inter-lead QRS dispersion [52]. In this study, we applied the same idea on the P-wave. In the new 3D vector space of the PCA, each lead was mapped to a vector in the new orthogonal axes constructed by the first 3 principle components (Fig. 5-6). We calculated the angles between each pair of the reconstructed vectors. A smaller angle indicates spatially closer vectors and vice versa. The differences in the angles in the AF group from the normal group represents a change in the inter-lead relationship, which indicates a shape distortion in the P-loop.

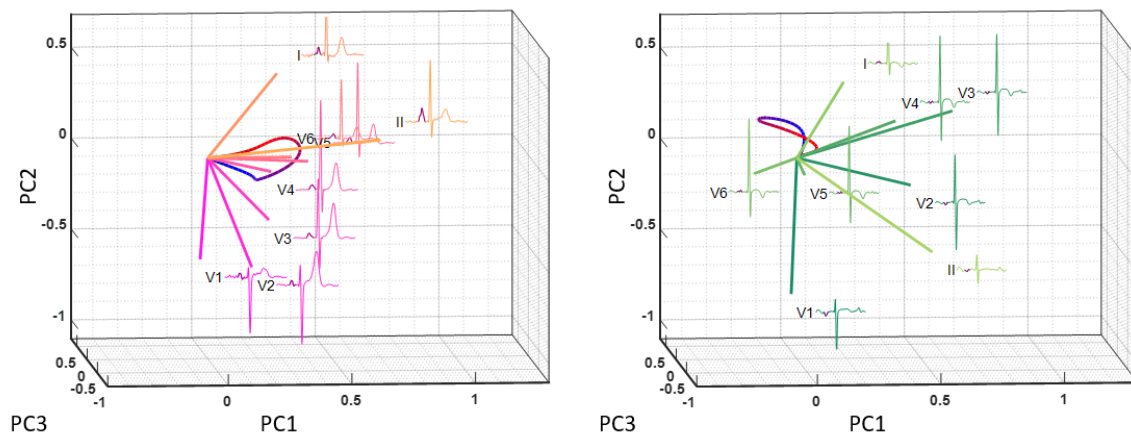
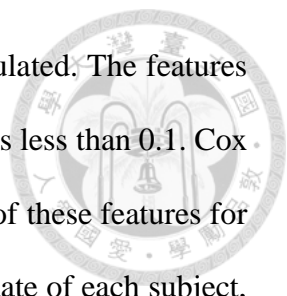


Figure 5- 6. The inter-lead correlation of the P-loop by PC1, PC2 and PC3. The left panel is an example from the control subject and the right panel is one subject from the AF group.

5.3.4 Statistical analysis

We compare the differences in mean (median) of all the extracted features in the AF and control groups with the independent student t-test when the assumption of normal distribution meets. If the assumption of normality fails by a p-value smaller than 0.05 with Shapiro-test, a non-parametric Wilcoxon rank-sum test was performed instead. To understand the predictability of these features, a logistic regression was performed and the



area under curve (AUC) of the receiver-operator curve (ROC) was calculated. The features were selected by sequential forward selection until the increase of AUC is less than 0.1. Cox proportional hazard model was used for assessing the time-dependency of these features for the risk of having AF in 3 months. The start point is the ECG examine date of each subject, and the end point is set to be the date of the ECG for the AF confirmation. For the control group, the end of observation is the date when the last ECG was recorded. To ensure balancing between AF and control group, recording times for more than 90 days in the normal group were censored to 90 days.

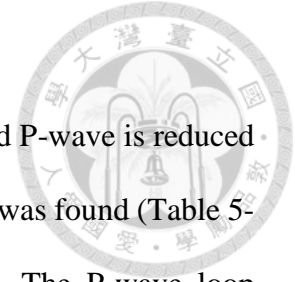
5.4 Statistical significance of the features

5.4.1 Morphology features

We found significant differences between AF and control patients (Table 5-1). The AF patients are characterized with a reduced amplitude in P-wave, R wave and T wave in limb leads, and a smaller T-wave amplitude and larger QRS interval in the chest leads. There is time-dependency in P-wave and QRS related features. A higher risk of AF is found in patients with larger P-wave duration, an earlier P-onset time (that is, a longer PR interval), a larger QRS interval, and a decreased height of ST segment.

Table 5- 1. Differences in morphology features for AF and control patients and the respective hazard ratio in cox survival analysis.

Feature	Number of samples		Measurement		Effect		Cox survival analysis		
	AF	Control	AF mean±SD	Control mean±SD	Size	P-value	cutoff point	Hazard ratio	P-value
<i>Limb leads</i>									
P_duration	203	240	0.133 ± 0.017	0.130 ± 0.015	0.173	0.072	0.129	1.542	0.002 **
P_peak position	199	234	0.251 ± 0.032	0.255 ± 0.023	-0.149	0.133	0.236	0.703	0.024 *
P_onset	201	236	0.182 ± 0.039	0.189 ± 0.027	-0.183	0.064	0.168	0.671	0.008 **
P_offset	199	234	0.318 ± 0.027	0.320 ± 0.023	-0.096	0.325	0.330	1.233	0.144
P wave amplitud	189	228	0.024 ± 0.034	0.031 ± 0.031	-0.216	0.030 *	0.010	0.747	0.053
R wave amplitud	203	242	0.590 ± 0.223	0.658 ± 0.253	-0.284	0.003 **	0.799	0.608	0.006 **
S wave amplitud	95	119	-0.189 ± 0.102	-0.189 ± 0.085	0.000	0.999	-0.249	0.827	0.410
T wave amplitud	197	232	0.063 ± 0.086	0.099 ± 0.084	-0.423	<0.001 ***	0.051	0.539	<0.001 ***
PR interval	193	240	148.031 ± 34.862	145.550 ± 27.916	0.080	0.422	154.000	1.238	0.142
QRS interval	196	228	88.929 ± 21.342	83.991 ± 14.359	0.275	0.006	92.000	1.375	0.037 *
QT interval	203	235	416.335 ± 44.011	411.906 ± 36.755	0.110	0.258	416.000	1.240	0.125
ST segment heigl	202	234	-0.053 ± 0.034	-0.058 ± 0.029	0.151	0.121	-0.046	1.443	0.010 *
<i>Chest leads</i>									
P wave amplitud	154	212	0.003 ± 0.046	0.000 ± 0.043	0.070	0.516	0.008	1.511	0.010 **
R wave amplitud	206	239	1.201 ± 0.574	1.204 ± 0.458	-0.006	0.948	0.907	0.769	0.073
S wave amplitud	175	209	-0.634 ± 0.376	-0.609 ± 0.318	-0.074	0.479	-0.811	0.817	0.236
T wave amplitud	193	238	0.113 ± 0.166	0.156 ± 0.162	-0.263	0.007 **	0.154	0.597	<0.001 ***
PR interval	160	214	153.638 ± 30.792	152.598 ± 24.882	0.038	0.727	172.000	1.328	0.108
QRS interval	194	220	89.062 ± 13.730	86.227 ± 7.564	0.260	0.011 *	92.000	1.680	0.001 ***
QT interval	206	243	413.728 ± 51.536	406.066 ± 33.930	0.179	0.069	434.000	1.626	0.001 **
ST segment heigl	198	228	-0.095 ± 0.061	-0.095 ± 0.046	0.002	0.985	-0.068	1.408	0.020 *



5.4.2 PCA related features

The weight of principle component 1 of the PCA on the extracted P-wave is reduced in AF patients, and a relatively higher weights in principle component 2 was found (Table 5-2). The weights of PC1 and PC 2 have both time-dependent effect. The P-wave loop expanded by PC1 and 2 also showed a smaller area in AF patients.

Table 5- 2. Differences in PCA related features for AF and control patients and the respective hazard ratio in cox survival analysis.

Feature	Number of samples		Measurement		Effect		Cox survival analysis		
	AF	Control	AF mean±SD	Control mean±SD	Size	P-value	cutoff point	Hazzard ratio	P-value
Loop Area	204	243	0.508 ± 0.091	0.511 ± 0.108	-0.029	0.756	0.560	0.692	0.016 *
Loop Length	188	217	271.691 ± 2.756	271.770 ± 2.691	-0.029	0.774	271.000	0.925	0.594
Loop L/A ratio	192	229	536.585 ± 89.121	538.885 ± 111.374	-0.023	0.814	491.104	1.454	0.014 *
weight of PC1	204	236	0.885 ± 0.085	0.917 ± 0.057	-0.451	<0.001 ***	0.920	0.621	0.001 ***
weight of PC2	205	235	0.106 ± 0.082	0.074 ± 0.053	0.469	<0.001 ***	0.077	1.433	0.010 **
weight of PC3	196	225	0.007 ± 0.005	0.006 ± 0.004	0.273	0.007	0.006	1.290	0.075

5.4.3 Inter-lead P-wave dispersion

We found a time-dependent effect on the risk of AF in the inter-lead angles (Table 5-3); larger angles between V2 and V3, Lead II and V2, Lead I and V2, and V2 and V6. A higher risk of AF was also present with larger angles between V3 and V6 and Lead I and V5, and a smaller angle between Lead II and V6.

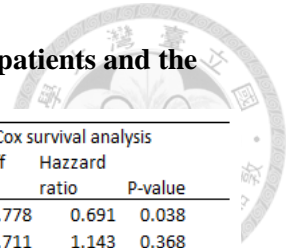


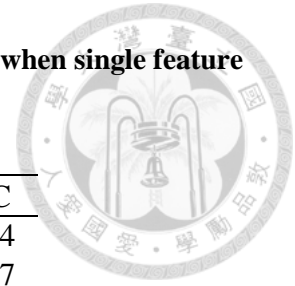
Table 5- 3. Differences in inter-lead P-wave dispersion for AF and control patients and the respective hazard ratio in cox survival analysis.

Inter-lead dispersion	Number of samples		Measurement		Effect		Cox survival analysis		
	AF	Control	AF mean±SD	Control mean±SD	Size	P-value	cutoff point	Hazard ratio	P-value
I_II	200	237	70.815 ± 14.864	72.617 ± 14.493	-0.123	0.202	82.778	0.691	0.038
II_V1	206	233	77.296 ± 10.080	76.743 ± 10.467	0.054	0.574	74.711	1.143	0.368
V1_V2	211	244	48.948 ± 24.077	52.321 ± 24.566	-0.139	0.141	71.708	0.768	0.115
V2_V3	211	244	40.767 ± 21.726	39.089 ± 20.732	0.079	0.402	42.599	1.324	0.042 *
V3_V4	202	242	30.872 ± 16.116	33.664 ± 19.767	-0.153	0.102	42.642	0.728	0.068
V4_V5	203	238	29.143 ± 17.606	29.195 ± 18.151	-0.003	0.975	17.318	1.315	0.086
V5_V6	204	239	28.807 ± 19.706	26.515 ± 16.657	0.126	0.191	29.004	1.237	0.132
I_V1	207	241	70.055 ± 17.131	67.407 ± 19.610	0.143	0.128	56.948	1.289	0.128
II_V2	205	226	75.187 ± 12.142	73.378 ± 12.576	0.146	0.129	79.618	1.412	0.013 *
V1_V3	210	238	69.837 ± 16.092	71.533 ± 14.621	-0.111	0.246	66.892	0.798	0.109
V2_V4	211	244	58.105 ± 20.865	55.898 ± 20.797	0.106	0.260	65.238	1.237	0.125
V3_V5	211	244	51.832 ± 20.928	49.941 ± 21.511	0.089	0.343	70.341	1.228	0.180
V4_V6	211	244	46.884 ± 22.857	45.165 ± 23.095	0.075	0.426	43.847	1.198	0.190
I_V2	203	238	74.219 ± 11.482	70.996 ± 13.662	0.254	0.007 **	77.015	1.337	0.038 *
II_V3	211	244	60.982 ± 21.731	62.393 ± 22.007	-0.065	0.492	59.223	0.802	0.111
V1_V4	205	231	76.183 ± 11.080	77.195 ± 9.265	-0.100	0.305	73.793	0.854	0.274
V2_V5	208	235	69.031 ± 15.696	67.404 ± 15.472	0.104	0.274	78.026	1.235	0.135
V3_V6	211	244	62.806 ± 19.795	60.580 ± 20.530	0.110	0.240	79.356	1.421	0.020 *
I_V3	208	240	71.367 ± 13.574	72.036 ± 13.770	-0.049	0.605	78.170	1.148	0.326
II_V4	211	244	58.183 ± 23.494	57.644 ± 23.001	0.023	0.806	68.509	1.124	0.402
V1_V5	201	238	76.532 ± 10.757	75.611 ± 9.714	0.090	0.351	82.866	1.485	0.007 **
V2_V6	203	237	71.750 ± 12.482	70.992 ± 14.271	0.056	0.553	62.932	1.408	0.046 *
I_V4	209	239	68.496 ± 17.756	69.910 ± 15.665	-0.085	0.375	58.347	0.790	0.121
II_V5	211	244	56.466 ± 25.277	61.048 ± 23.208	-0.189	0.046	49.524	0.796	0.105
V1_V6	205	237	72.463 ± 12.329	72.822 ± 12.657	-0.029	0.763	76.759	0.847	0.238
I_V5	211	244	60.337 ± 21.734	58.468 ± 21.311	0.087	0.357	72.715	1.343	0.037 *
II_V6	211	244	56.489 ± 22.750	63.462 ± 21.059	-0.319	0.001 ***	71.970	0.646	0.003 **
I_V6	211	244	51.566 ± 24.206	50.439 ± 23.486	0.047	0.616	71.377	1.225	0.187

5.5. Classification of AF and control patients

We performed logistic regressions for each of the variable and see the AUC of ROC for each variable. Table 5-4 lists the top 10 biomarkers for identify AF patients, and the most important feature is the amplitude of T-wave on the limb lead which yields an AUC of 0.61 (Fig. 5-7). The other biomarkers including weight of PC1, PC2 and the T-wave amplitude on the chest leads. In the stepwise inclusion of all the candidate variables, the final AUC can reach 0.67 (Fig. 5-8), and the contributing variables include T wave amplitude (limb leads), angle between II and V6, R wave amplitude (limb leads), angle between V1 and V2, and P wave duration (Table 5-5).

Table 5- 4. The top 10 features for classifying the AF and control subjects when single feature is used.



Rank	Variable	AUC
1	T wave amplitude (limb)	0.614
2	Weight of PC1	0.597
3	Weight of PC2	0.594
4	Angle: II_V6	0.589
5	T wave amplitude (chest)	0.572
6	Angle: II_V2	0.565
7	R wave amplitude (limb)	0.561
8	P wave duration	0.555
9	Angle I_V2	0.553
10	Weight of PC3	0.551

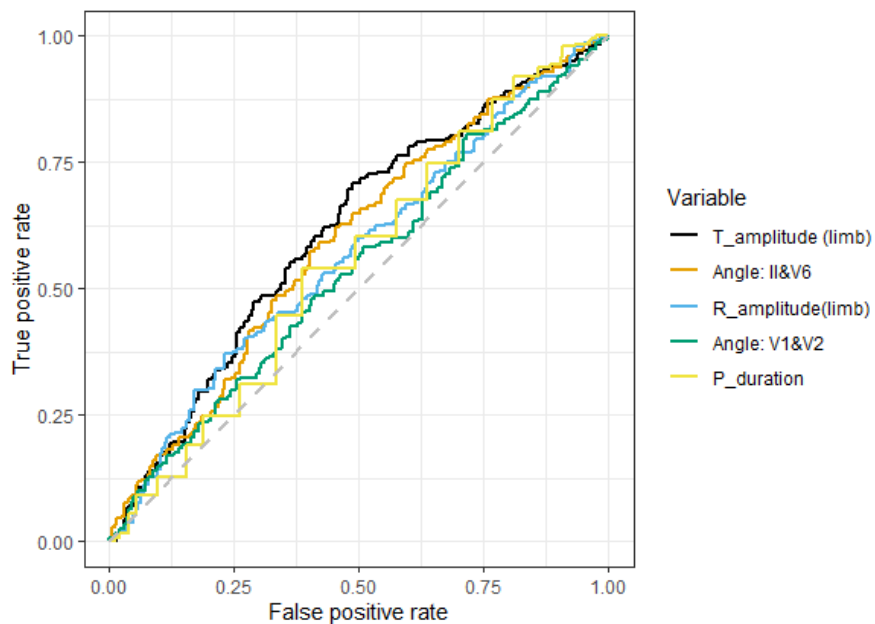


Figure 5- 7. The ROCs for classifying AF patients by single variable.



Table 5- 5. The first 5 selected feature for classifying AF patients using stepwise forward selection in the logistic regression.

Rank	Variable	AUC
1	T wave amplitude (limb)	0.614
2	Angle: II and V6	0.634
3	R wave amplitude (limb)	0.651
4	Angle: V1 and V2	0.662
5	P wave duration	0.672

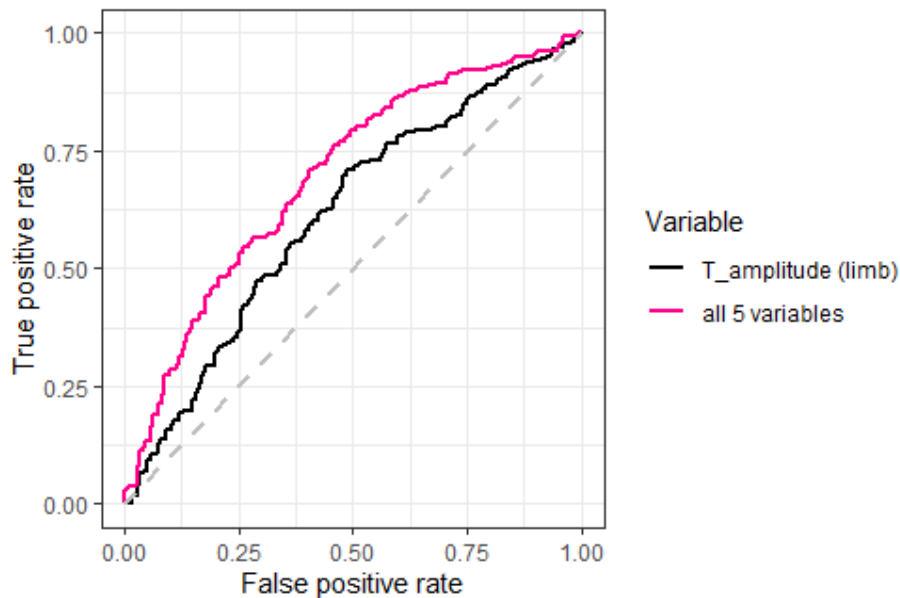


Figure 5- 8. The ROC for classifying AF with combined variables.

5.6 Discussion and implication

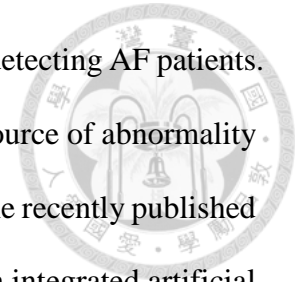
In this study, we have developed an algorithm that is able to isolate P-wave, which reflects electrical activity of the atrial, from 12-lead ECG. We have shown that, when transforming the 12-lead with the PCA which represents the individualized P-wave axis, the inter-lead relationships on this new axis can be quantified. The inter-lead relationships and

the PCA weighting are promising biomarkers for AF, which showed a significant difference between the AF and control group. With the features derived from PCA of the extracted P-wave, specifically the angles between the physical leads, the ability of detecting potential AF patients can increase at least 10% than the traditional morphology features.

When classifying the AF and control group by logistic regression, the prominent biomarker is the T-wave amplitude. The reduced T-wave amplitude is observed in the AF patients, and patients with a T-amplitude less than 0.051 mV has a hazard ratio equal to 1.8 times. The T-wave amplitude represents ventricular repolarization, and a decrease or deflection may have related with ischemia [53]. Ischemia and myocardial infarction are known risk factors for atrial fibrillation due to ischemia or hemodynamic changes in atrial stretch [54, 55]. In our results, we also found ST-segment to be a significant risk factor in the cox survival analysis which showed a 1.4 times higher risk, though there is no significantly different between AF and control group. The comorbidity of ischemia can be further investigated by the medical history. The other explanation of the reduced T-wave amplitude is the additional depolarization activities from the atrial that contaminate the derived ECG. This can also explain the reduced P-wave and R-wave amplitudes in the AF patients.

The weighting of the PC1 and PC2 is also highly significantly different between the AF and non-AF groups, showing a transmission energy dispersion in the abnormal atrial. These two variables alone are the most prominent feature when prediction AF except the T-wave amplitude. However, they are not present in the stepwise inclusion procedure of feature selection, indicating a dependency on the T-wave amplitude. On the other hand, the inter-lead dispersion of P-wave, specifically the angles between lead II and V6 and between V1 and V2, are independent factors that contribute to the detection of AF.

Our finding showed a limited power on the proposed features in detecting AF patients. As the pathology of AF is the fibrosis of any area of the atria, a single source of abnormality or single lead distortion may not be detected from a cohort of patients. The recently published work incorporated 180922 patients with 454789 ECGs and trained by an integrated artificial system may be holistic view of pathology of the AF, and therefore reaches an AUC of 0.87 [50]. Our work here can be combined with the detailed medical history or the ablation outcomes to provide clinical insights.



Chapter 6. Extension to step function



6.1 Generalized algorithm

In Sec. 4.5, we demonstrated the use of our MA-EMD on several spike-contaminated datasets. Here, we extend our method to the removal of step-function signal components. To better describe the idea in a real implementation and avoid confusion with numerical differentiation and integration, we use the discrete-time representation of the signal, $x[t]$. Because the first derivative of a Heaviside step function is a spike, we can approximate the first derivative of the signal $x(t)$ by a finite difference, that is, $\tilde{x}[t] = x[t] - x[t - 1]$. The signal $\tilde{x}[t]$ can be decomposed into IMFs using MA-EMD. The first mode, $\tilde{c}[t]$, is the signal with the spike (step function). By subtracting $\tilde{c}[t]$ from $\tilde{x}[t]$, we obtain $\tilde{x}_2[t]$ as the first-order time-difference of the step-function-removed signal. Finally, we can reconstruct the step-function-removed signal $x_2[t]$ using the cumulative summation (approximating the integration) of $\tilde{x}_2[t]$, i.e., $x_2[t] = \sum_{s=0}^t \tilde{x}_2[s]$. The proposed workflow is given in Algorithm 5. In fact, Algorithm 5 can easily be generalized to handle any function whose N^{th} -order derivative is a spike function, for example, the Heaviside step function or a sigmoid function with a steep change in slope.

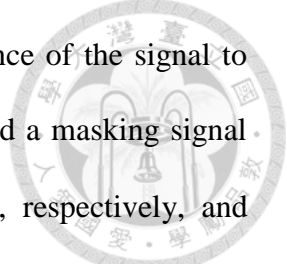


Algorithm 5: Removing step function by MA-EMD

- (1) Input signal $x[t]$
 - (2) Take the time-difference of the input signal $\tilde{x}[t] = x[t] - x[t - 1]$
 - (3) Perform MA-EMD on $\tilde{x}[t]$. Let $\tilde{c}[t]$ be the first IMF, which is
 - (4) (3-1) Define $\tilde{x}'[t] = \tilde{x}[t]$.
 - (5) (3-2) Identify spikes in $\tilde{x}'[t]$. These spikes should correspond to the points on the step function.
 - (6) (3-3) Apply the minimum arclength criteria of (11) and (12). Find the replacements for the spike points in the local maxima Γ_x to obtain the upper envelope $U(t)$.
 - (7) (3-4) Perform step (4) in Algorithm I and derive $h[t]$.
 - (8) (3-5) If the stopping criteria in step (5) in Algorithm I are met, assign $\tilde{c}[t] = h[t]$ as the IMF and go to (4). Otherwise, let $\tilde{x}'[t] = h[t]$, and repeat (3-2) to (3-4).
 - (9) Calculate $\tilde{x}_2[t] = \tilde{x}[t] - \tilde{c}[t]$.
 - (10) Let $x_2[t] = \sum_{s=0}^t \tilde{x}_2[s]$. Then, $x_2[t]$ is the step-removed signal.
-

6.2 Example: Photoplethysmogram (PPG) recording

To describe the use of Algorithm II, we utilize a photoplethysmogram (PPG) recording from a transmittance pulse oximeter recorded at 256 Hz as an example. When estimating the blood oxygen saturation level (SpO_2) from the PPG, it is necessary to calculate the amplitude variation (AC) of the pulsatile component of the PPG waveform [56]. The PPG waveform often suffers from baseline drift and noise, and it is necessary to filter the signal using a bandpass filter with a passband ranging from 0.5 to 5 Hz [57, 58] before calculating the AC. In our recording, there is contamination of the step function owing to a change in the DC gain from either an LED light emission or firmware calibration (Fig. 6-1(a)). This step function in the signal obtained after applying a 0.5–5 Hz bandpass filter results in a large spread of data distortion for approximately five pulses (Fig. 6-1(c)).



According to Algorithm II, we take the first-order time-difference of the signal to form $\tilde{x}[t]$, and the step function thus becomes a spike function. We add a masking signal $S_M^k[t] = a_M \cos[2\pi f_M t + 2\pi k/K]$ in which a_M and f_M are 1 and 20, respectively, and consider $K = 2$ realizations. Then, for each realization, we use MA-EMD on $\tilde{x}^k[t] = \tilde{x}[t] + S_M^k[t]$ to extract the first IMF, $\tilde{c}^k[t]$, where the spike resides. The spike function of $\tilde{x}[t]$ is then calculated by averaging all $\tilde{c}^k[t]$, i.e., $\tilde{c}[t] = \sum_{k=1}^K \tilde{c}_k[t]$. Finally, the reconstructed signal $x_2[t]$ is processed using a cumulative summation of the spike-removed signal $\tilde{x}_2[t] = \tilde{x}[t] - \tilde{c}[t]$. The detailed flow chart for the processing of this example is exhibited in Fig. 6-2. In fact, this flow chart can represent a general algorithm dealing with the step functions in any type of signal. The set of minimum impulses, G , is the step function. The masking signal is not necessary but is suggested so as to limit the band width of the derived first IMF. The frequency and amplitude of the masking signal should be determined through Eqs. (4-1) and (4-7).

In contrast, the conventional EMD alone can also be treated as an adaptive filter to replace the bandpass filter. In this study, we also tested the ability of the conventional EMD in dealing with this problem as a comparison. Because IMFs 1–3 carry most of the 0.5–5 Hz components (Fig. 6-1(d)) and IMF 4 and later modes are contaminated by the step function, we treat the summation of IMFs 1–3 as a signal filtered through EMD.

The signal reconstructed by our MA-EMD is shown in Fig. 6-1(a). When filtered by the same 0.5–5 Hz bandpass filter, the distortion reduces to only 1–3 pulses (Fig. 6-1(c)). Comparatively, when we directly apply EMD to the original PPG signal as an adaptive filter, the results also show a distortion near the location where the step function occurs, and the

effected range is approximately five pulses, which is not smaller than that achieved using a Fourier bandpass filter (Fig. 6-1(c)).

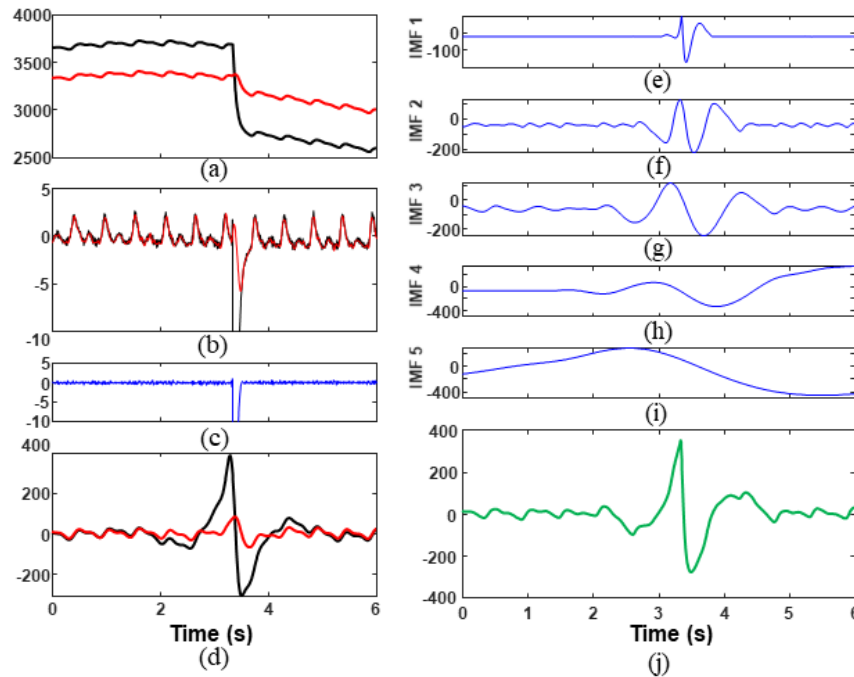


Figure 6- 1. Step function removal in PPG using MA-EMD.

(a) Original PPG $x[t]$ (black) and step-removed PPG $x_3[t]$ (red). (b) First-order time-difference of signals, i.e., $\tilde{x}[t]$ (black) and spike (step)-removed signal, $\tilde{x}_2[t]$ (red). (c) Extracted spike function in $\tilde{x}[t]$. (d) Band-pass-filtered PPG signals of $x[t]$ (black) and $\tilde{x}_2[t]$ (red). (e-j) IMFs 1–5 (blue line) when applying conventional EMD on $x[t]$ and the summation of IMFs 1–3 (green).

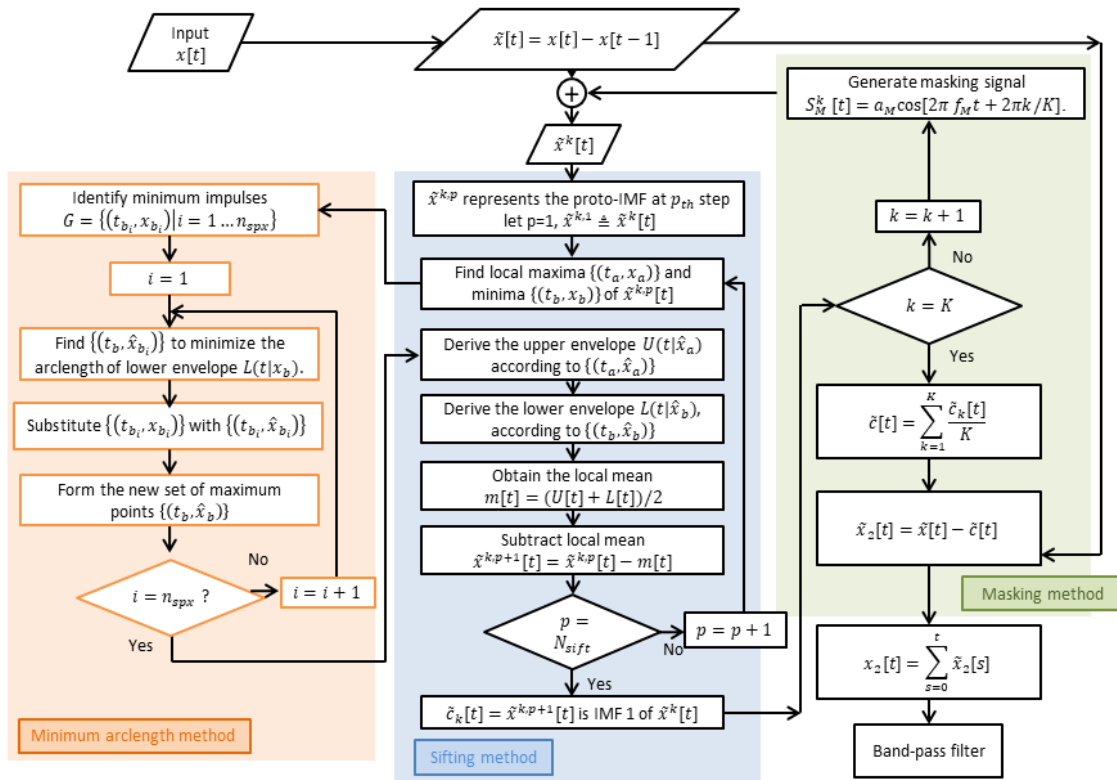
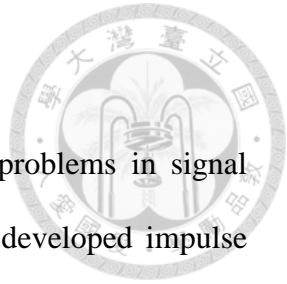


Figure 6- 2. Flowchart for removing step functions in the PPG signal.

Chapter 7. Conclusion

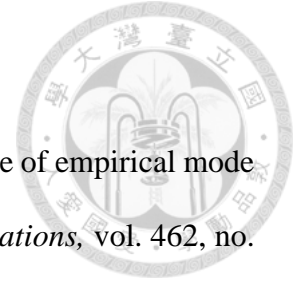


Nonstationary impulse noise and step functions are common problems in signal processing and disrupt the IMFs of EMD. By introducing a recently developed impulse response theory of decomposition, we clarified that the sifting process is effectively a non-stationary highpass filter whose cut-off frequency depends on the extrema interlacing interval. There are mainly two causes of the undesirable effects of spikes in EMD. First, the extremely large impulse response by the spike point. Second, the newly generated extrema. The interaction of these two results in a locally high-frequency oscillation distinct from the signal at other locations. This results in a chain of effects of non-stationary mode-splitting which propagates throughout the IMFs.

In order to overcome this problem, our MA-EMD finds a replacement point of the spike that minimizes the number of newly generated extrema and reduces the impulse response from the spike. This way, the spike can be fully attributed to and isolated in the first IMF, and as a result the latter IMFs would be free from this disturbance. A mathematical proof and two numerical simulations are provided. To further facilitate the spike extraction, masking-aided MA-EMD (MAMA-EMD) is proposed. Aided with a masking signal with proper frequency and amplitude, we isolate the spikes in the first IMF, and improve the performance of decomposition the later IMFs. We also provided a mathematical induction and numerical experiment to find the proper amplitude and frequency of masking signal. We applied the MAMA-EMD method on the ECG to isolate the P-wave which represents atrial activity, and showed the statistical significance of the P-wave related

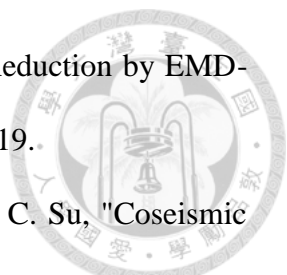
features in identifying potential AF patients. Finally, we proposed a general algorithm for separating the Heaviside step function by applying our MA-EMD approach.

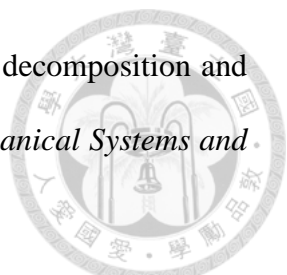
Future applications to signals whose N^{th} -order derivative is a spike function can be expected. We believe that we have established a solution to an important problem regarding the nonstationary noise incurred during EMD. The proposed MA-EMD can further be applied to other EMD modifications, resulting in a robust algorithm for stationary and nonstationary types of noise.

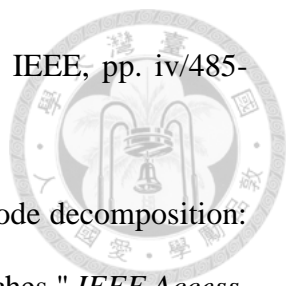



Bibliography

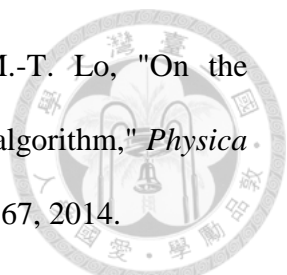
- [1] Y.-H. Wang, H.-W. V. Young, and M.-T. Lo, "The inner structure of empirical mode decomposition," *Physica A: Statistical Mechanics and its Applications*, vol. 462, no. 300, pp. 1003-1017, 2016.
- [2] N. Huang, Z. Shen, S. Long, M. Wu, and H. Shih, "The empirical mode decomposition and the Hilbert spectrum for nonlinear and non-stationary time series analysis," *Proceedings of the Royal Society A-Mathematical Physical and Engineering Sciences*, vol. 454, pp. 903-995, 1998, doi: 10.1098/rspa.1998.0193.
- [3] I. Daubechies, J. Lu, and H. T. Wu, "Synchrosqueezed wavelet transforms: An empirical mode decomposition-like tool," *Applied and Computational Harmonic Analysis*, vol. 30, no. 2, pp. 243-261, 2011, doi: 10.1016/j.acha.2010.08.002.
- [4] J. Gilles, "Empirical wavelet transform," *IEEE Transactions on Signal Processing*, vol. 61, no. 16, pp. 3999-4010, 2013, doi: 10.1109/TSP.2013.2265222.
- [5] C. Zhuang and P. Liao, "An Improved Empirical Wavelet Transform for Noisy and Non-Stationary Signal Processing," *IEEE Access*, vol. 8, pp. 24484-24494, 2020, doi: 10.1109/ACCESS.2020.2968851.
- [6] K. Dragomiretskiy and D. Zosso, "Variational Mode Decomposition," *IEEE TRANSACTIONS ON SIGNAL PROCESSING*, vol. 62, no. 3, 2014, doi: 10.1109/TSP.2013.2288675.
- [7] L. Zǎo, R. Coelho, and P. Flandrin, "Speech Enhancement with EMD and Hurst-Based Mode Selection," vol. 22, no. 5, pp. 899-911, 2014.

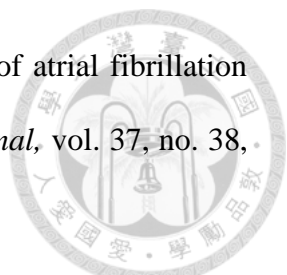
- 
- [8] W. Shen, Y. Yu, L. Ling, J. Ren, and Q. Zhu, "Speech Noise Reduction by EMD-LMS," pp. 485-488, 2020, doi: 10.1109/iccsnt47585.2019.8962419.
- [9] J. Y. Huang, K. L. Wen, X. J. Li, J. J. Xie, C. T. Chen, and S. C. Su, "Coseismic deformation time history calculated from acceleration records using an EMD-derived baseline correction scheme: A new approach validated for the 2011 Tohoku earthquake," *Bulletin of the Seismological Society of America*, vol. 103, no. 2 B, pp. 1321-1335, 2013, doi: 10.1785/0120120278.
- [10] P. Nguyen and J. M. Kim, "Adaptive ECG denoising using genetic algorithm-based thresholding and ensemble empirical mode decomposition," *Information Sciences*, vol. 373, pp. 499-511, 2016, doi: 10.1016/j.ins.2016.09.033.
- [11] E. Alickovic, J. Kevric, and A. Subasi, "Performance evaluation of empirical mode decomposition, discrete wavelet transform, and wavelet packed decomposition for automated epileptic seizure detection and prediction," *Biomedical Signal Processing and Control*, vol. 39, pp. 94-102, 2018, doi: 10.1016/j.bspc.2017.07.022.
- [12] M. B. Hossain, S. K. Bashar, A. J. Walkey, D. D. McManus, and K. H. Chon, "An Accurate QRS Complex and P Wave Detection in ECG Signals Using Complete Ensemble Empirical Mode Decomposition with Adaptive Noise Approach," *IEEE Access*, vol. 7, pp. 128869-128880, 2019, doi: 10.1109/ACCESS.2019.2939943.
- [13] H. Li, Y. Hu, F. Li, and G. Meng, "Succinct and fast empirical mode decomposition," *Mechanical Systems and Signal Processing*, vol. 85, pp. 879-895, 2017, doi: 10.1016/j.ymsp.2016.09.031.

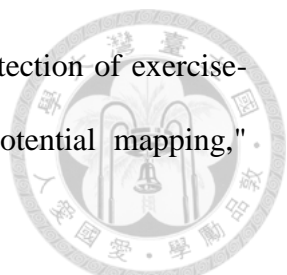
- 
- [14] J. Zheng, J. Cheng, and Y. Yang, "Generalized empirical mode decomposition and its applications to rolling element bearing fault diagnosis," *Mechanical Systems and Signal Processing*, vol. 40, pp. 136-153, 2013.
- [15] F. Xu, X. Song, K. L. Tsui, F. Yang, and Z. Huang, "Bearing Performance Degradation Assessment Based on Ensemble Empirical Mode Decomposition and Affinity Propagation Clustering," *IEEE Access*, vol. 7, pp. 54623-54637, 2019, doi: 10.1109/ACCESS.2019.2913186.
- [16] A. E. Prosvirin, M. M. M. Islam, and J.-M. Kim, "An Improved Algorithm for Selecting IMF Components in Ensemble Empirical Mode Decomposition for Domain of Rub-Impact Fault Diagnosis," *IEEE Access*, vol. 7, pp. 121728-121741, 2019, doi: 10.1109/access.2019.2938367.
- [17] Z. Wu and N. E. Huang, "Ensemble empirical mode decomposition: a noise-assisted data analysis method," *Advances in Adaptive Data Analysis*, vol. 1, no. 1, pp. 1-41, 2009.
- [18] J.-R. Yeh, J.-S. Shieh, and N. E. Huang, "Complementary ensemble empirical mode decomposition: a novel noise enhanced data analysis method," *Advances in Adaptive Data Analysis*, vol. 2, no. 2, pp. 135-156, 2010, doi: 10.1142/S1793536910000422.
- [19] M. E. Torres, M. A. Colominas, G. Schlotthauer, and P. Flandrin, "A complete ensemble empirical mode decomposition with adaptive noise," *ICASSP, IEEE International Conference on Acoustics, Speech and Signal Processing - Proceedings*, pp. 4144-4147, 2011, doi: 10.1109/ICASSP.2011.5947265.
- [20] R. Deering and J. F. Kaiser, "The use of a masking signal to improve empirical mode decomposition," in *Proceedings.(ICASSP'05). IEEE International Conference on*

- 
- Acoustics, Speech, and Signal Processing, 2005.*, 2005, vol. 4: IEEE, pp. iv/485-iv/488 Vol. 4.
- [21] Y. H. Wang, K. Hu, and M. T. Lo, "Uniform phase empirical mode decomposition: An optimal hybridization of masking signal and ensemble approaches," *IEEE Access*, vol. 6, pp. 34819-34833, 2018, doi: 10.1109/ACCESS.2018.2847634.
- [22] J. Zheng, H. Pan, T. Liu, and Q. Liu, "Extreme-point weighted mode decomposition," *Signal Processing*, vol. 142, pp. 366-374, 2018, doi: 10.1016/j.sigpro.2017.08.002.
- [23] H. Li, L. Yang, and D. Huang, "The study of the intermittency test filtering character of Hilbert-Huang transform," *Mathematics and Computers in Simulation*, vol. 70, pp. 22-32, 2005, doi: 10.1016/j.matcom.2005.03.020.
- [24] X. Hu, S. Peng, and W. L. Hwang, "EMD revisited: A new understanding of the envelope and resolving the mode-mixing problem in AM-FM signals," *IEEE Transactions on Signal Processing*, vol. 60, no. 3, pp. 1075-1086, 2012, doi: 10.1109/TSP.2011.2179650.
- [25] C. Wang, Q. Kema, and F. Da, "Regenerated Phase-Shifted Sinusoid-Assisted Empirical Mode Decomposition," vol. 23, no. 4, pp. 556-560, 2016.
- [26] G. Rilling and P. Flandrin, "One or two frequencies? The empirical mode decomposition answers," *IEEE Transactions on Signal Processing*, vol. 56, no. 1, pp. 85-95, 2008.
- [27] Z. Wang and D. Zhang, "Progressive switching median filter for the removal of impulse noise from highly corrupted images," *IEEE Transactions on Circuits and Systems II: Analog and Digital Signal Processing*, vol. 46, no. 1, pp. 78-80, 1999, doi: 10.1109/82.749102.

- 
- [28] J. Chen, Y. Zhan, and H. Cao, "Adaptive Sequentially Weighted Median Filter for Image Highly Corrupted by Impulse Noise," *IEEE Access*, vol. 7, no. i, pp. 158545-158556, 2019, doi: 10.1109/ACCESS.2019.2950348.
- [29] H. Hwang and R. A. Haddad, "Adaptive Median Filters: New Algorithms and Results," *IEEE Transactions on Image Processing*, vol. 4, no. 4, pp. 499-502, 1995.
- [30] H. Qiu, J. Lee, J. Lin, and G. Yu, "Wavelet filter-based weak signature detection method and its application on rolling element bearing prognostics," *Journal of Sound and Vibration*, vol. 289, no. 4-5, pp. 1066-1090, 2006.
- [31] Z. Nenadic and J. W. Burdick, "Spike detection using the continuous wavelet transform," *Ieee Tbme*, vol. 52, no. 1, pp. 74-87, 2005. [Online]. Available: <http://www.ncbi.nlm.nih.gov/pubmed/15651566>.
- [32] R. C. Nongpiur, "Impulse Noise Removal in Speech Using Wavelets," 2008, 3 ed., pp. 1593-1596.
- [33] N. E. Huang, Z. Shen, and S. R. Long, "A new view of nonlinear water waves: the Hilbert spectrum 1," *Annu. Rev. Fluid Mech*, vol. 31, pp. 417-57, 1999.
- [34] M. Unser, "Splines: A perfect fit for signal processing," 2000, doi: 10.1109/79.799930.
- [35] F. Ehrentreich and L. Summchen, "Spike removal and denoising of Raman spectra by wavelet transform methods," *Analytical Chemistry*, vol. 73, no. 17, pp. 4364-4373, 2001.
- [36] S. R. Kim and A. Efron, "Adaptive robust impulse noise filtering," *IEEE Transactions on Signal Processing*, vol. 43, no. 8, pp. 1855-1866, 1995.

- 
- [37] Y.-H. Wang, C.-H. Yeh, H.-W. V. Young, K. Hu, and M.-T. Lo, "On the computational complexity of the empirical mode decomposition algorithm," *Physica A: Statistical Mechanics and its Applications*, vol. 400, pp. 159-167, 2014.
- [38] H. W. Yang *et al.*, "A Minimum arclength method for removing spikes in empirical mode decomposition," *IEEE Access*, vol. 7, pp. 13284-13294, 2019, doi: 10.1109/ACCESS.2019.2892622.
- [39] J. H. Ahn, D. H. Kwak, and B. H. Koh, "Fault detection of a roller-bearing system through the EMD of a wavelet denoised signal," *Sensors (Switzerland)*, vol. 14, no. 8, pp. 15022-15038, 2014.
- [40] J. Lee, H. Qiu, G. Yu, J. Lin, and R. T. Services, "IMS Bearing Data," ed, 2007.
- [41] L. Parrino, R. Ferri, O. Bruni, and M. G. Terzano, "Cyclic alternating pattern (CAP): The marker of sleep instability," *Sleep Medicine Reviews*, vol. 16, no. 1, pp. 27-45, 2012, doi: 10.1016/j.smr.2011.02.003.
- [42] M. G. Terzano *et al.*, "Atlas, rules, and recording techniques for the scoring of cyclic alternating pattern (CAP) in human sleep," *Sleep Medicine*, vol. 2, pp. 537-553, 2001, doi: 10.1016/S1389-9457(01)00149-6.
- [43] A. L. Goldberger *et al.*, "PhysioBank, PhysioToolkit, and PhysioNet: Components of a New Research Resource for Complex Physiologic Signals," *Circulation*, vol. 101, no. 23, pp. e215-e220, 2000.
- [44] H. Zulkifly, G. Y. Lip, and D. A. Lane, "Epidemiology of atrial fibrillation," *International journal of clinical practice*, vol. 72, no. 3, p. e13070, 2018.
- [45] T. M. Munger, "Atrial fibrillation," *Journal of Biomedical Research*, vol. 28, no. 1, pp. 1-17, 2014, doi: 10.7555/jbr.28.20130191.

- 
- [46] P. Kirchhof *et al.*, "2016 ESC Guidelines for the management of atrial fibrillation developed in collaboration with EACTS," *European Heart Journal*, vol. 37, no. 38, pp. 2893-2962, 2016, doi: 10.1093/eurheartj/ehw210.
- [47] C.-H. Tseng *et al.*, "Cloud-Based Artificial Intelligence System for Large-Scale Arrhythmia Screening," *Computer*, vol. 52, no. 11, pp. 40-51, 2019, doi: 10.1109/mc.2019.2933195.
- [48] I. Savelieva and A. J. Camm, "Clinical relevance of silent atrial fibrillation: prevalence, prognosis, quality of life, and management," *Journal of Interventional Cardiac Electrophysiology*, vol. 4, no. 2, pp. 369-382, 2000.
- [49] H. Kottkamp, "Human atrial fibrillation substrate: towards a specific fibrotic atrial cardiomyopathy," *European heart journal*, vol. 34, no. 35, pp. 2731-2738, 2013.
- [50] Z. I. Attia *et al.*, "An artificial intelligence-enabled ECG algorithm for the identification of patients with atrial fibrillation during sinus rhythm: a retrospective analysis of outcome prediction," *The Lancet*, vol. 394, no. 10201, pp. 861-867, 2019, doi: 10.1016/s0140-6736(19)31721-0.
- [51] P. Laguna, R. Jané, and P. Caminal, "Automatic detection of wave boundaries in multilead ECG signals: Validation with the CSE database," *Computers and biomedical research*, vol. 27, no. 1, pp. 45-60, 1994.
- [52] W.-H. Hsieh *et al.*, "A novel noninvasive surface ECG analysis using interlead QRS dispersion in arrhythmogenic right ventricular cardiomyopathy," *PloS one*, vol. 12, no. 8, 2017.

- 
- [53] H. Hanninen *et al.*, "ST-T integral and T-wave amplitude in detection of exercise-induced myocardial ischemia evaluated with body surface potential mapping," *Journal of electrocardiology*, vol. 36, no. 2, pp. 89-98, 2003.
- [54] A. D. Krahn, J. Manfreda, R. B. Tate, F. A. Mathewson, and T. E. Cuddy, "The natural history of atrial fibrillation: incidence, risk factors, and prognosis in the Manitoba Follow-Up Study," *The American journal of medicine*, vol. 98, no. 5, pp. 476-484, 1995.
- [55] H. Watanabe *et al.*, "ST-segment abnormalities and premature complexes are predictors of new-onset atrial fibrillation: the Niigata preventive medicine study," *American heart journal*, vol. 152, no. 4, pp. 731-735, 2006.
- [56] L. J. Mengelkoch, D. Martin, and J. Lawler, "A review of the principles of pulse oximetry and accuracy of pulse oximeter estimates during exercise," *Physical Therapy*, vol. 74, no. 1, pp. 40-49, 1994, doi: 10.1093/ptj/74.1.40.
- [57] B. Sangeeta and S. Laxmi, "A real time analysis of PPG signal for measurement of SpO₂ and pulse rate," *International Journal of Computer Applications*, vol. 36, no. 11, pp. 45-50, 2011.
- [58] P. Madhan Mohan, A. Annie Nisha, V. Nagarajan, and E. Smiley Jeya Jothi, "Measurement of arterial oxygen saturation (SpO₂) using PPG optical sensor," *International Conference on Communication and Signal Processing, ICCSP 2016*, pp. 1136-1140, 2016, doi: 10.1109/ICCSP.2016.7754330.